Nonlinear Dyn (2025) 113:28179–28206
https://doi.org/10.1007/s11071-025-11568-4

RESEARCH

Feature preserving discretization of memristive circuits using an input-output approach

Giacomo Innocenti · Alberto Tesi · Mauro Di Marco · Luca Pancioni · Mauro Forti

Received: 3 April 2025 / Accepted: 1 July 2025 / Published online: 1 August 2025

Abstract It is known that continuous-time (CT) dynamic analog circuits containing ideal memristors and, more generally, memelements, admit for structural reasons first integrals and, consequently, enjoy the *foliation feature* of the state space. This important property makes it possible the coexistence of a huge number of different attractors, even when the memelement has a constitutive relation of a general shape. This paper considers the problem of how discrete-time (DT) memristive circuits preserving this foliation feature can be derived by the CT ones. Specifically, a discretization procedure of CT circuits is proposed in input-output setting, instead of the state space one, which applies to memristors as well as memcapacitors and meminductors, and it is not limited to the Forward Euler discretization operator. It is shown that the procedure provides DT maps which preserve the foliation feature of the original CT circuits for any discretization time step T, thus enabling extreme multistability. Moreover, it is highlighted that by increasing the time step T the obtained DT maps can exhibit chaotic attractors even if the CT memristive circuits display convergent behaviors, a phenomenon which is known as computational chaos. As an example, it is shown that, by applying the proposed procedure to a simple CT RC-memristive circuit with the memristor charge depending quadratically on the flux, the obtained DT circuits embed the logistic and the Henon maps depending on the chosen discretization operator.

Keywords Memristive circuit · Discretization · Invariant manifold · Computational chaos

G. Innocenti (✉) · A. Tesi
Department of Information Engineering, University of Florence, via di S. Marta 3, 50139 Firence, FI, Italy
e-mail: giacomo.innocenti@unifi.it

A. Tesi
e-mail: alberto.tesi@unifi.it

M. Di Marco · L. Pancioni · M. Forti
Department of Information engineering and mathematics, University of Siena, via Roma, 56, 53100 Siena, SI, Italy
e-mail: mauro.dimarco@unisi.it

L. Pancioni
e-mail: luca.pancioni@unisi.it

M. Forti
e-mail: mauro.forti@unisi.it

1 Introduction

The memristor (memory resistor) was theorized by L.O. Chua in his seminal paper [1] as the fourth basic passive circuit element, in addition to the resistor, capacitor, and inductor. However, the interest in memristors emerged only many years later thanks to the memristive effects discovered in nanotechnology devices by Williams and his team [2]. This finding also led to the introduction of memcapacitors and meminductors [3], the two memelements modeling memory effects in capacitors and inductors, respectively. Since those years, the research activity on memelements has rapidly increased generating a literally huge number

of contributions in several directions, mainly because they are expected to play a prominent role in futuristic neuromorphic computers [4–9].

One relevant research branch concerns the investigation of continuous-time (CT) dynamic analog circuits containing ideal memristors and, more generally, memelements, although their relationship with real devices showing memory effects has not been completely disclosed yet. Indeed, due to their memory and nonlinearity, memelements are able to greatly enrich the range of circuit dynamic behaviors, a feature which is crucial for employing analog circuits in future electronics [10–15]. This richness of dynamic behaviors stems from the fact that they enjoy the *foliation feature*, i.e the state space is composed by a continuum of invariant manifolds and the initial conditions determine the invariant manifold where the circuits dynamics is constrained to lie (see [16,17] and references therein). The foliation feature has important consequences on the dynamics of CT memristive circuits since it ensures that convergent behaviors as well as oscillatory and chaotic behaviors are robust with respect to the invariant manifolds, i.e. if one of these behaviors is displayed on an invariant manifold, then the same type of behavior is expected on nearby invariant manifolds. For instance, this can lead to the coexistence of infinitely many oscillatory and chaotic behaviors that can be controlled by appropriately setting the initial conditions via pulse programmed sources (see [18] and references therein). Furthermore, the dynamics shown on more distant manifolds can be very different, ranging from convergent behaviors to oscillations and more complex attractors. Summing up, these circuits can generate a huge number of different coexisting attractors for a fixed configuration of the circuit parameters, a peculiar dynamic property often referred to as extreme multistability, and can exhibit the so-called phenomenon of bifurcations without parameters [19–22].

Recently, increasing attention has been paid to discrete-time (DT) memristive circuits derived from CT memristive circuits. One reason for this increasing interest relies on the fact that real memristive devices for laboratory experiments are still not always readily available and hence DT models can be used to set up digital emulators to investigate the dynamic performance of CT memristive circuits (see, e.g., [23–25]). Indeed, emulators based on DT maps can be directly implemented on digital computers or other types of digital signal processors, such as ASIC (application-specific integrated circuit) and FPGA (field-programmable gate array). Another reason stems from the fact that DT maps can generate a much richer dynamics than the CT counterparts. This was first observed in [26] where it is clearly shown how a second order DT map, derived by a simple sampling switch-based memristor-capacitor circuit, is capable to generate very complex dynamics while the original CT circuit is not. Since then, several contributions have shown that these maps are not only capable to display chaos and hyperchaos, as well as extreme multistability, but can also potentially be useful for engineering applications in relevant fields, such as secure communications, image and video encryption and random number generation [27–37]. However, less attention has been paid to how maps can be derived from CT memristive circuits, as the typical procedure is to directly apply the Forward Euler integration method to the state equations of the CT circuit. Despite its simplicity, this procedure does not generally preserve the characteristic of the first integrals of the original CT circuits (see, e.g., [37]). This appears as a limitation because the loss of the foliation feature reduces somewhat the possibility of displaying coexistence of different attractors, especially if the memristor nonlinear characteristic is not of the sine type (see, e.g., [32,35]). Very recently, a new discretization procedure of the state space equations has been introduced in [38] to ensure that first integrals are preserved independently of the discretization time step. Based on this procedure, it is shown that the derived DT circuits show the existence of invariant manifolds in the state space and the related phenomena of extreme multistability and bifurcations without parameters [39–41].

The goal of this paper is to extend this recent approach in several directions: i) the discretization procedure considers an input-output description of CT circuits instead of the state space one; ii) the procedure applies to memristors as well as memcapacitors and meminductors, along with mild assumptions on their constitutive relations; iii) the procedure is not limited to the Forward Euler method but considers a large variety of numerical integration methods. Specifically, we consider the class of CT circuits depicted in Fig. 1 that is composed by a linear time-invariant two-terminal element (one port) connected to a memelement. The linear element contains linear R, L, C components, ideal operational amplifiers, controlled sources and is characterized by either its

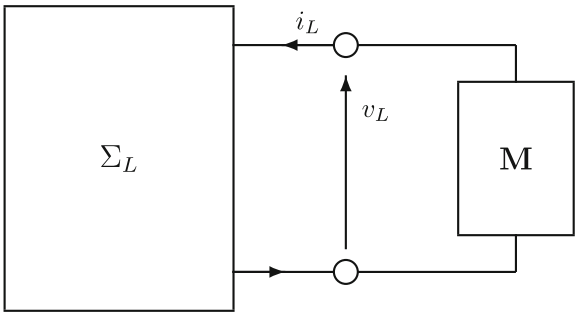

Fig. 1 The class of circuits: Σ_L is a linear time-invariant two-terminal element (one port) with input current i_L and voltage v_L; **M** is either a memristor or a memcapacitor or a meminductor

impedance or admittance. The memelement can be a flux-controlled or charge-controlled memristor, a flux-controlled or charge momentum-controlled capacitor, a flux momentum-controlled or charge-controlled inductor, and its constitutive relation is assumed to be sufficiently smooth. In [18,42] it has been shown that the dynamics of any circuit of this class, independently of the type of memelement, obeys a nonlinear differential equation which admits first integrals and, consequently, enjoys the foliation feature of the phase-space. Starting from this point, we develop a discretization procedure based on first replacing the time derivative operator with a discretization operator $\Delta(T, h_T)$, with T and h_T being the discretization time step and the continuous-time T-ahead shift operator, respectively. Specifically, $\Delta(T, h_T)$ is assumed to be a rational function of h_T which approximates the time derivative operator as T goes to zero and satisfies $\Delta(T, h_T) f(t) = 0$ for any constant function $f(t)$. These assumptions are indeed satisfied by several discretization operators, including classic ones as Forward Euler, backward Euler, and Tustin methods as well as single-stage multi-step, multi-stage single-step, and averaging techniques. Then, it is shown that the maps of the DT circuits, obtained by simply substituting h_T with the DT one-step-ahead shift operator h, preserve the first integrals feature of the original CT circuits for any discretization time step T. Hence, the phase-space of these maps is composed by a continumum of invariant manifolds where different dynamics can be displayed, thus possibly giving rise to extreme multistability and computational chaos. The term computational chaos was coined by Edward N. Lorenz in [43] with reference to the fact that when one seeks approximate solutions of a set of differential equations by stepwise numerical integration, the choice of a not sufficiently small T may yield chaotic solutions, even when the true CT solutions approach limit cycles or equilibrium points.

The rest of the paper is organized as follows. Section 2 introduces notations, definitions and preliminaries used throughout the paper. A CT circuit composed by the interconnection of an RC two-terminal element and a flux-controlled memristor is employed as a motivating example in Section 3, also to illustrate how the proposed discretization procedure ensures that the foliation feature of the CT circuit is preserved. Section 4 contains the problem formulation showing that the dynamics of any circuit of the considered class is described by a nonlinear differential equation which admits first integrals and, hence, a phase-space composed by a continuum of invariant manifolds. The new discretization procedure is discussed in Section 5, showing that it provides DT maps which preserve first integrals for any discretization time step and a large class of discretization operators, whose derivation is reported in Appendix A for completeness. Section 6 analyzes the dynamics of the maps obtained by applying the procedure to the CT circuit of Section 3 with the flux-controlled memristor replaced by a flux momentum-controlled meminductor. The dependance of the dynamics of the DT maps upon the discretization time step T and the discretization operator $\Delta(T, h_T)$ is discussed in Section 7, also investigating when, by properly selecting T and $\Delta(T, h_T)$, the CT circuit of Section 3 generates the logistic and Henon maps . Some conclusions end the paper in Section 8.

2 Mathematical background

2.1 Notation

- $\mathbb{C}, \mathbb{R}, \mathbb{Z}, \mathbb{Z}_+$: complex set, real set, integer set, positive integer set
- $s \in \mathbb{C}, t \in \mathbb{R}, k \in \mathbb{Z}$: complex variable, continuous-time (CT) variable, discrete time (DT) variable
- $\mathcal{D}$: time-derivative operator $\frac{d}{dt}$
- $\mathcal{D}^i f(t)$: value assumed by the i-th derivative of function f at time t
- $\mathcal{C}^i(\mathbb{R})$: class of functions continuous on $\mathbb{R}$ up to the i-th derivative
- $R(x)$: polynomial function of $x \in \mathbb{R}$

- order$[R(x)]$: maximum power of the polynomial function R
- Φ: nonlinear function of the constitutive relation of the memelement
- Ψ: nonlinear characteristic function of the phase-space model of the memelement
- T: discretization time step
- h_T: CT T-ahead shift operator
- h: DT one-step-ahead shift operator
- $\Delta(T, h_T)$: CT discretization operator
- $\Delta_T(h)$: DT operator

2.2 Definitions and preliminaries

In this section we introduce definitions and preliminaries used throughout the paper.

Definition 1 For a given integrable function $g(t) : \mathbb{R} \to \mathbb{R}$, all the functions $f(t) : \mathbb{R} \to \mathbb{R}$ such that

$$\mathcal{D} f(t) = g(t) \tag{1}$$

are referred to as *primitives* of g and can be expressed as

$$f(t) = f(t_0) + \mathcal{D}^{-1}_{[t_0]} g(t) \,,$$

where $\mathcal{D}^{-1}_{[t_0]} g(t) := \int_{t_0}^{t} g(\tau) d\tau$.

For the sake of simplicity, in the paper the primitives of g will sometimes be referred to as simply $\mathcal{D}^{-1}_{[t_0]} g(t)$, omitting their specific value at $t = t_0$, when it is not strictly necessary for the characterization or the understanding of the result.

In the paper, the two-terminal element Σ_L in Fig. 1 is described via a linear time-invariant differential equation of the following form

$$R(\mathcal{D}) f(t) = S(\mathcal{D}) g(t) \tag{2}$$

where $f(t) : \mathbb{R} \to \mathbb{R}$ and $g(t) : \mathbb{R} \to \mathbb{R}$ are such that $f(t) = i_L(t)$ and $g(t) = v_L(t)$ or $f(t) = v_L(t)$ and $g(t) = i_L(t)$, and $R(\mathcal{D})$ and $S(\mathcal{D})$ are two polynomial functions of $\mathcal{D}$ with real coefficients. Notice that, by applying the Laplace transform to (2), we get that $R(s)/S(s)$, with s being the complex variable, is the impedance or the admittance of Σ_L. Throughout the paper we always assume that order$[R(\mathcal{D})] >$ order$[S(\mathcal{D})]$ and, for the sake of simplicity, we sometimes omit the explicit dependence on t of $f(t)$ and $g(t)$.

Now, we formally define some known operators to be used later.

Definition 2 For any $T > 0$ and any function $f(t) : \mathbb{R} \to \mathbb{R}$, the CT *$T$-ahead shift operator* h_T is defined so that

$$h_T f(t) = f(t + T) \,, \quad \forall t \in \mathbb{R} \,. \tag{3}$$

For any sequence $\{x_k\}_{k \in \mathbb{Z}} \subset \mathbb{R}$, the *DT one-step-ahead shift operator* h is defined so that

$$h x_k = x_{k+1} \,, \quad \forall k \in \mathbb{Z} \,. \tag{4}$$

The operators h_T and h enjoy the following shift properties:

$$\begin{cases} h_T^k f(t) = f(t + kT) \,, \forall t \in \mathbb{R} \,, \forall k \in \mathbb{Z} \\ h^i x_k = x_{k+i} \,, \qquad \forall k \in \mathbb{Z} \,, \forall i \in \mathbb{Z} \,. \end{cases} \tag{5}$$

The next definition introduces operators depending on h_T and T which approximate $\mathcal{D}$.

Definition 3 Any operator $\Delta(T, h_T)$ such that

$$\lim_{T \to 0^+} [\Delta(T, h_T) f(t)] = \mathcal{D} f(t) \,, \quad \forall t \in \mathbb{R} \tag{6}$$

for any function of time $f(t) : \mathbb{R} \to \mathbb{R}$ that is t-differentiable (almost) everywhere is said to be a *CT discretization operator*.

The accuracy of any discretization operator is defined via the residual equation:

$$\Delta(T, h_T) f(t) - \mathcal{D} f(t) = o(T^\eta) \,, \quad \eta \in \mathbb{Z}_+ \,, \tag{7}$$

where the little-o term $o(T^\eta)$ means that the error in approximating $\mathcal{D} f(t)$ with $\Delta(T, h_T) f(t)$ vanishes faster than T^η, i.e.,

$$\lim_{T \to 0^+} \left[\frac{\Delta(T, h_T) f(t) - \mathcal{D} f(t)}{T^\eta} \right] = 0 \,. \tag{8}$$

In Section 5.2 we recall several discretization operators which are rational functions of h_T with coefficients

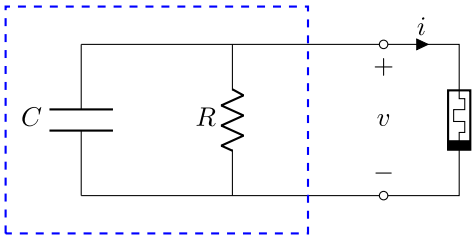

Fig. 2 The circuit studied in Section 3: the blue box highlights the two-terminal element Σ_L; v and i are the memristor voltage and current

depending on T. As an example, in the Forward Euler case

$$\Delta(T, h_T) = \frac{h_T - 1}{T}$$

and (7) holds with $\eta = 1$.
The next definition associates a DT operator depending on h and T to each discretization operator.

Definition 4 For any sequence $\{x_k\}_{k\in\mathbb{Z}} \subset \mathbb{R}$, the *DT operator* $\Delta_T(h)$ is defined so that

$$\Delta_T(h)x_k = \Delta(T, h)x_k \ , \quad \forall k \in \mathbb{Z} \ .$$

Observe that $\Delta_T(h)$ is obtained by formally substituting $h_T \leftarrow h$ in the discretization operator, and hence it inherits the structure of $\Delta(T, h_T)$. This also suggests that it can be seen as an operator approximating the derivative, i.e., such that $\Delta_T(h)x_k \approx \mathcal{D}x(t)$ for $t = kT$, under the assumption that x_k is close to the sample of $x(t)$ at $t = kT$.

3 Motivating Example: *RC*-memristive circuit

Consider the circuit in Fig. 2 where the two-terminal element Σ_L, made out of the parallel of a resistor R and a capacitor C, is connected to an ideal flux-controlled memristor, whose charge $q(t)$ and flux $\varphi(t)$ are linked by the nonlinear function $\Phi : \mathbb{R} \to \mathbb{R}$ defining the constitutive relation $q(t) = \Phi\big(\varphi(t)\big)$.
The two-terminal element Σ_L is described by the linear time-invariant differential equation

$$\left(\mathcal{D} + \frac{1}{RC}\right) v(t) = -\frac{1}{C} i(t) \ ,$$

whose solution $v(t)$ for $t \geq t_0$ depends on the initial condition $v(t_0)$, other than the input $i(t)$. Observe that Σ_L can be formally written as

$$v(t) = -L(\mathcal{D})i(t) \ , \tag{9}$$

where

$$L(\mathcal{D}) = \frac{\frac{1}{C}}{\mathcal{D} + \frac{1}{RC}} \ , \tag{10}$$

and that $L(s)$, with s being the complex variable, is the impedance of Σ_L.
The phase-space model of the flux-controlled memristor is defined by the following equations

$$\begin{cases} \mathcal{D}\varphi(t) = v(t) \\ i(t) = \Psi(\varphi)v(t) \ , \end{cases} \tag{11}$$

where the flux $\varphi(t)$ is the phase-variable and $\Psi\big(\varphi(t)\big)$ is the nonlinear characteristic function of the model, known as mem-conductance. The solutions $\varphi(t)$ and $i(t), t \geq t_0$, depend on the initial condition $\varphi(t_0)$, other than the input v. It is known that $\Psi\big(\varphi(t)\big)$ is equal to the derivative with respect to $\varphi(t)$ of the function $\Phi\big(\varphi(t)\big)$. i.e.

$$\mathcal{D}\Phi\big(\varphi(t)\big) = \Psi\big(\varphi(t)\big)v(t) \ . \tag{12}$$

Observing that the first equation in (11) ensures that $\varphi(t)$ is a primitive of $v(t)$, it follows that

$$i(t) = \mathcal{D}\Phi\left(\mathcal{D}^{-1}_{[t_0]} v(t)\right) \ . \tag{13}$$

Substituting (13) into (9) and taking into account that where the term $\mathcal{D}$ has been collected because $v(t) = \mathcal{D}\varphi(t)$ and $i(t) = \mathcal{D}\Phi\big(\varphi(t)\big)$, it turns out that the circuit of Fig. 2 obeys the following nonlinear differential equation

$$\mathcal{D}\left(\left(\mathcal{D} + \frac{1}{RC}\right)\varphi(t) + \frac{1}{C}\Phi(\varphi(t))\right) = 0 \ . \tag{14}$$

Observe that (14) highlights the existence of first integrals which are given by

$$\left(\mathcal{D} + \frac{1}{RC}\right)\varphi(t) + \frac{1}{C}\Phi\big(\varphi(t)\big) = \mu \ , \tag{15}$$

where $\mu \in \mathbb{R}$ is a constant depending of the circuit initial conditions $\varphi(t_0)$ and $v(t_0) = \mathcal{D}\varphi(t_0)$, i.e., $\mu = v(t_0)+\varphi(t_0)/(RC)+\Phi(\varphi(t_0))/C$. This implies that the RC-memristive circuit enjoys the *foliation feature* that means that the state space, i.e. the $(\varphi, v = \mathcal{D}\varphi)$-plane in this case, is composed by a continuum of invariant manifolds of the following form

$$v + \frac{1}{RC}\varphi(t) + \frac{1}{C}\Phi\big(\varphi(t)\big) = \mu \,. \tag{16}$$

Indeed, each vector $(\varphi, v = \mathcal{D}\varphi)$ belongs to a unique manifold with μ satisfying (16), and the set of vectors obtained by varying $\mu \in \mathbb{R}$ is exactly the entire $(v = \mathcal{D}\varphi, \varphi)$-plane. Moreover, the dynamics generated by the circuit initial conditions $\varphi(t_0)$ and $v(t_0) = \mathcal{D}\varphi(t_0)$ evolves on the manifold (16) with $\mu = v(t_0) + \varphi(t_0)/(RC)+\Phi(\varphi(t_0))/C$ according to the differential equation (15).
To fix the ideas, assume that

$$\Phi(\varphi) = \gamma_1\varphi + \gamma_2\varphi^2 + \gamma_3\varphi^3 \tag{17}$$

and consider the circuit configuration

$$R = 1 \quad C = 1 \quad \gamma_1 = -5 \quad \gamma_2 = 0 \quad \gamma_3 = 1. \tag{18}$$

From (16) it follows that the invariant manifolds are shaped as cubic curves of the form

$$v = 4\varphi - \varphi^3 + \mu.$$

Clearly, by varying $\mu \in \mathbb{R}$, these cubic curves cover the entire $(v = \mathcal{D}\varphi, \varphi)$-plane, whose foliated structure is depicted in Fig. 3.
From (15) it follows that the dynamics on the manifold with index μ obeys the following differential equation

$$\mathcal{D}\varphi = 4\varphi - \varphi^3 + \mu.$$

It turns out that the equilibrium points are given by $(\varphi, v = \mathcal{D}\varphi) = (\varphi_P, 0)$ with φ_P such that $\varphi_P^3 - 4\varphi_P = \mu$. This implies that the entire φ-axis of the $(v = \mathcal{D}\varphi, \varphi)$-plane is made of non-isolated equilibrium points. Moreover, it can be checked that they are stable if $|\varphi_P| > \frac{2}{\sqrt{3}}$ and unstable when $|\varphi_P| < \frac{2}{\sqrt{3}}$. Therefore, the dynamics is multi-stable and it exhibits an infinite number of non-isolated attractors.

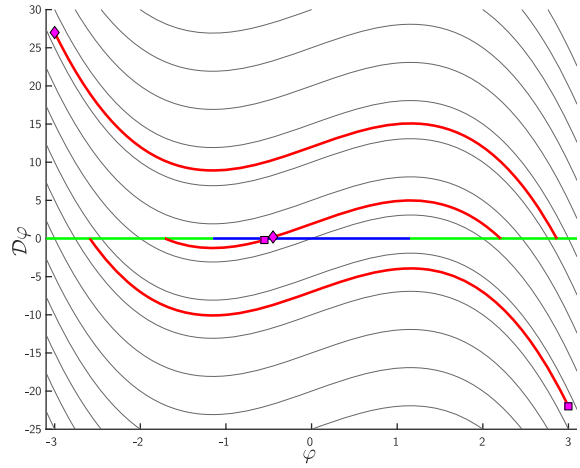

Fig. 3 The phase-space of circuit (14) is composed by a continuum of non-isolated invariant manifolds (foliation feature). Gray: examples of invariant manifolds. The initial conditions determine the invariant manifold where the trajectory is constrained to move. Red: examples of trajectories; diamonds and squares depict the initial conditions. Blue/green: unstable/stable equilibrium points that repel/attract the trajectories on the related invariant manifolds

Our goal is to set up a discretization procedure to design DT maps able to preserve the first integral structure, i.e. the foliation feature of the phase-space. First, we expand and rewrite (14) as

$$\begin{cases} \Theta\,(t) = \mathcal{D}\varphi(t) + \dfrac{1}{RC}\varphi(t) + \dfrac{1}{C}\Phi(\varphi(t)) \\ \mathcal{D}\Theta\,(t) = 0 \end{cases} . \tag{19}$$

The second equation in (19) confirms the existence of first integrals, since

$$\Theta\,(t) = \Theta\,(t_0) = \mu \,, \quad \forall t \geq t_0 \,, \tag{20}$$

while the first equation, with $\Theta(t)$ replaced by μ, describes the dynamics on the invariant manifold of index μ. Then, we substitute the time-derivative $\mathcal{D}$ in (19) with a discretization operator $\Delta(T, h_T)$. To fix the ideas, we consider the Forward Euler operator, i.e.,

$$\Delta(T, h_T) = \frac{h_T - 1}{T} \,, \tag{21}$$

whose residual equation (7) holds with $\eta = 1$, i.e. the error converges to zero faster than T. So doing, we obtain the two new T-parametric equations

$$\begin{cases} \Theta_d(t) = \dfrac{\varphi_d(t+T)-\varphi_d(t)}{T} + \dfrac{1}{RC}\varphi_d(t) \\ \qquad + \dfrac{1}{C}\Phi(\varphi(t)) \\ \dfrac{\Theta_d(t+T)-\Theta_d(t)}{T} = 0 \end{cases} \tag{22}$$

where the functions $\Theta_d(t)$ and $\varphi_d(t)$ have been introduced to stress that the solution of system (22) does not coincide with that of system (19), even though they approach each other when $T \to 0^+$, because $\Delta(T, h_T) \to \mathcal{D}$. Notice that the second equation of (22) is exactly equivalent to (20), thus highlighting that the substitution of $\mathcal{D}$ with $\Delta_T(T, h_T)$ preserves the invariant manifold structure for all $T > 0$. Finally, by assuming $t = kT$ and denoting $\Theta_k = \Theta_d(kT)$ and $\varphi_k = \varphi_d(kT)$, the second equation boils down to $\Theta_{k+1} = \Theta_k$, i.e., Θ_k is constant over k, while the first equation in (22) yields the following relationship

$$\Theta_k = \frac{1}{T}\varphi_{k+1} + \left(\frac{1}{RC} - \frac{1}{T}\right)\varphi_k + \frac{1}{C}\Phi(\varphi_k) = \bar{\mu}\ , \tag{23}$$

where the constant value $\bar{\mu}$ of the sequence $\{\Theta_k\}$, $k \in \mathbb{Z}$, can be derived from the circuit initial conditions at $t = t_0$, as it was done for μ in (15). Indeed, it can be readily checked that the relationship $\Theta_{k+1} = \Theta_k$ and the map defined by the second equality in (23) can be derived by directly using the DT operator $\Delta_T(h)$ obtained by replacing h_T with h in (21), i.e. $\Delta_T(h) = (h-1)/T$.

Summing up, the procedure for obtaining maps which preserve first integrals consists in simply replacing $\mathcal{D}$ with $\Delta_T(h)$ and $\varphi(t)$ with φ_k in (14). This leads to the following equation

$$\frac{h-1}{T} \times \underbrace{\left(\frac{1}{T}\varphi_{k+1} + \left(\frac{1}{RC} - \frac{1}{T}\right)\varphi_k + \frac{1}{C}\Phi(\varphi_k)\right)}_{[\star]} = 0 \tag{24}$$

where, according to (23), for any $\bar{\mu}$, equation $[\star] = \bar{\mu}$ defines a dynamics evolving on the manifold indexed by $\bar{\mu}$ itself. By rearranging all the terms of (24) and properly switching index k, we get the explicit DT map

$$\varphi_{k+1} = \varphi_k + \left(1 - T\frac{1}{RC}\right)(\varphi_k - \varphi_{k-1}) - \frac{T}{C}\left(\Phi(\varphi_k) - \Phi(\varphi_{k-1})\right) \tag{25}$$

Figure 4 reports some examples of invariant manifolds $[\star] = \bar{\mu}$ for the case of the nonlinear characteristic (17) and the circuit configuration (18). Also, it illustrates the behavior of map (25) for different initial conditions and values of T. The two sequences (red and blue) converge towards fixed points for $T = 0.015$, show a periodic behavior for $T = 0.040$ and $T = 0.055$, display a chaotic behavior for $T = 0.070$. In all cases, the evolution of the map remains on the invariant manifold to which the initial conditions belong.

Observe that (25) resembles the dynamics (14) only locally, since φ_k are the samples of the function $\varphi_d(t)$ solving (22), which differs from the solution $\varphi(t)$ of (14). In general, the difference evolves depending on both the used discretization technique and the contracting properties of the field around the considered solution of the CT circuit. Figures 5A and B report, for the configuration (17)-(18), the solution $\varphi(t)$ of (14) whose initial conditions are depicted as diamonds and squares in Fig. 3. They are plotted against the sequences generated by (25) for different values of T, but initialized at equivalent starting points. As expected, the sequences approximate $\varphi(t)$ better as T converges to zero.

Finally, it is important to underline that the first integral structure of (14) would have been lost if the form $i(t) = \Psi\big(\varphi(t)\big)v$ in (11) was used in place of (13). Indeed, in that case from (9) we get the input-output model

$$\left(\mathcal{D} + \frac{1}{RC}\right)\mathcal{D}\varphi(t) + \frac{1}{C}\Psi\big(\varphi(t)\big)\mathcal{D}\varphi(t) = 0 \tag{26}$$

and, since the operators $\Psi\big(\varphi(t)\big)$ and $\mathcal{D}\varphi(t)$ do not commute, it is not possible to collect $\mathcal{D}$ and ensure the foliation feature of the phase-space anymore.

In this respect, we can show that the foliation feature is not preserved with the standard approach used in the literature (see, e.g., [28–31]) to obtain DT maps from CT memristive circuits. In that approach the DT maps are derived by simply applying the Forward Euler method to the state space model of the CT circuit. In the case of the RC-memristive circuit of Fig. 2 we get the following DT map

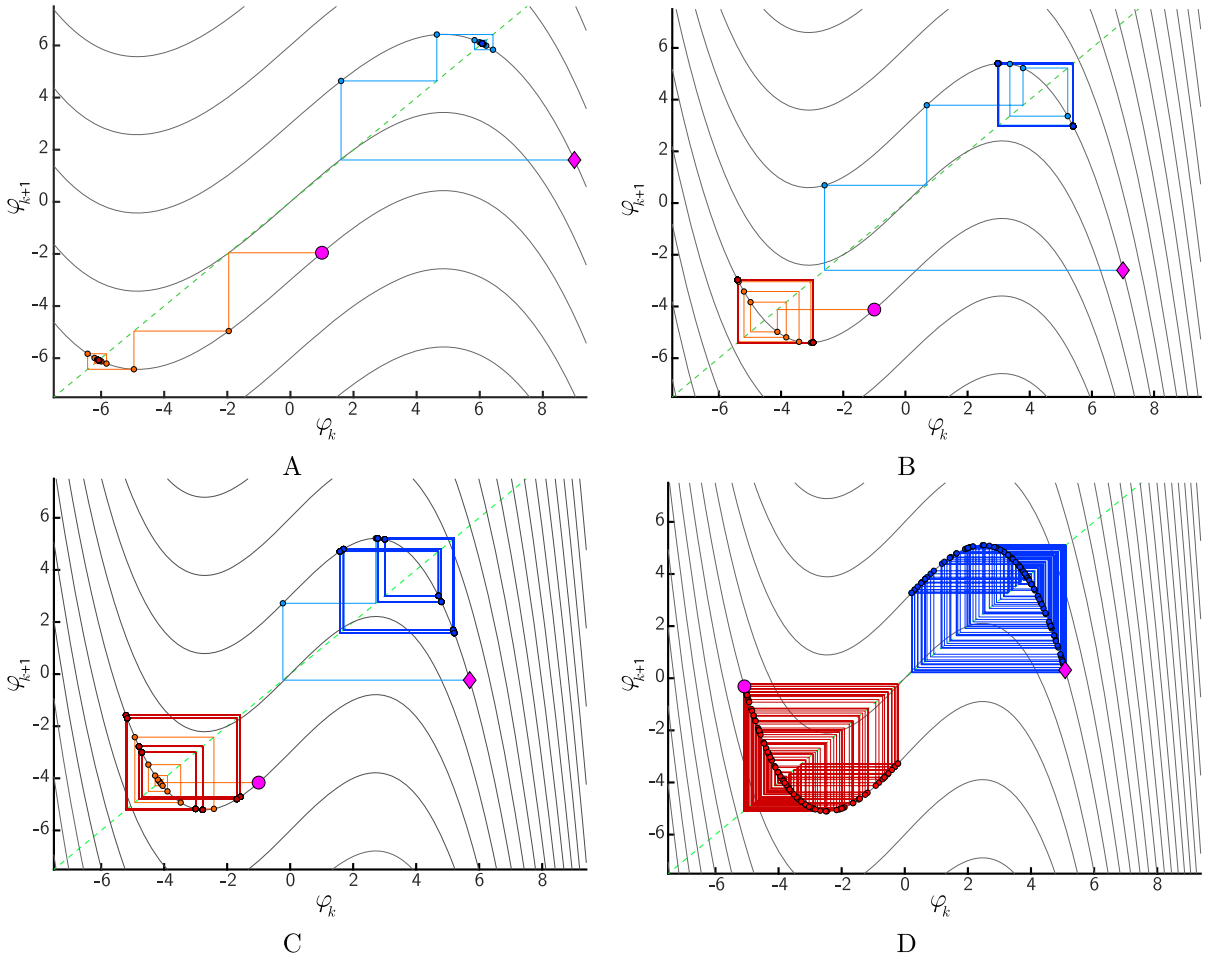

Fig. 4 Phase-space of map (25) for $T = 0.015$ (A), $T = 0.040$ (B), $T = 0.055$ (C), and $T = 0.070$ (D). Solid Grey: Examples of invariant manifolds. The evolution of the map, whose initial conditions belong to a certain invariant manifold, is bound to stay there forever. Red dots: The evolution of the map initialized from the magenta circle. Blue dots: The evolution starting from the magenta diamond. Dashed green: the phase-space bisector. The sequences of states (drawn as dots) starting from initial conditions placed on different manifolds, i.e., the magenta circle and diamond, have been highlighted using solid lines of the same color of the dots

$$\begin{cases} v_{k+1} = \left(1 - \frac{T}{RC}\right) v_k - \frac{T}{C} \Psi(\varphi_k) v_k \\ \varphi_{k+1} = \varphi_k + T v_k \end{cases}, \tag{27}$$

where Ψ is the mem-conductance. From the second equation of (27) we get $v_k = \frac{1}{T}(\varphi_{k+1} - \varphi_k)$, that, substituted into the first one and after properly switching index k, leads to the explicit DT map

$$\varphi_{k+1} = \varphi_k + \left(1 - T\frac{1}{RC}\right)(\varphi_k - \varphi_{k-1}) - \frac{T}{C} \underbrace{\left(\Psi(\varphi_{k-1})\varphi_k - \Psi(\varphi_{k-1})\varphi_{k-1}\right)}_{[*]}, \tag{28}$$

It can be checked that (28) is indeed the DT map obtained by substituting $\mathcal{D}$ with $(h - 1)/T$ in the input-out model (26). A direct comparison highlights that (28) differs from (25), which admits infinitely many invariant manifolds. Indeed, the model (28) does not enjoy such a feature, because the term $[*]$ cannot be written as the difference of some quantity at step $k + 1$ and the same quantity at step k, as instead it happens for the last term of equation (25).

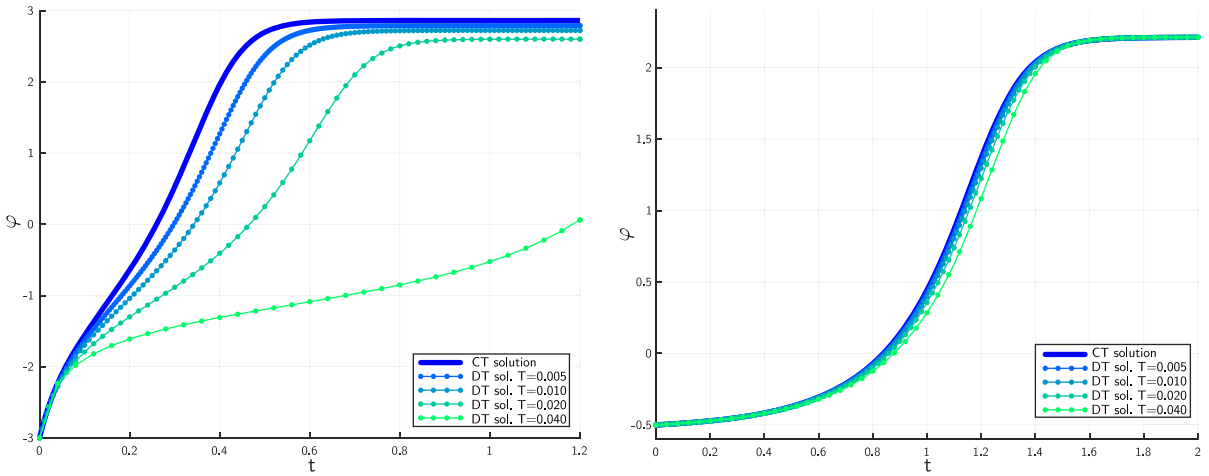

Fig. 5 Comparison between the solutions of the CT equation system (19) and the sequences of DT map (25). The DT solutions are obtained for different values of T, ranging from $T = 0.005$ to $T = 0.040$. A: The CT trajectory has been initialized at the higher magenta diamond of Fig. 3. In order to relate the DT sequences and the CT solution, they have been initialized using the first two samples of this latter. B: The CT trajectory has been initialized at the lower magenta square of Fig. 3

4 Problem Set Up

Our goal is to extend and generalize the procedure presented in [38] to create DT maps from the CT memristive circuit in Fig. 1 preserving the *foliation feature* of the state space and hence capable to display multistable behaviors and bifurcations without parameters on their infinitely many invariant manifolds (see [16,17]).
First, we observe the two-terminal element Σ_L is described by the linear differential equation

$$R(\mathcal{D})v_L - S(\mathcal{D})i_L = 0 \tag{29}$$

for two properly defined polynomial functions $R(\mathcal{D})$ and $S(\mathcal{D})$. Formally, we can rewrite (29) as

$$v_L = \frac{S(\mathcal{D})}{R(\mathcal{D})} i_L = L(\mathcal{D})i_L \tag{30}$$

and

$$i_L = \frac{R(\mathcal{D})}{S(\mathcal{D})} v_L = \bar{L}(\mathcal{D})v_L \ , \tag{31}$$

where the rational functions $L(\mathcal{D})$ and $\bar{L}(\mathcal{D})$ clearly satisfy $L(\mathcal{D})\bar{L}(\mathcal{D}) = 1$. Notice that the rational functions $L(s)$ and $\bar{L}(s)$, with s being the complex variable, represent the impedance and the admittance of Σ_L, respectively. Hereafter, we will refer to (30) as the impedance input-output model of Σ_L, and to (31) as its admittance input-output model.

Consider now the six ideal memelements which, for the sake of simplicity, are hereafter identified by the bold codes in the first column of Table 1. We denote by v_M and i_M their voltage and current using the passive sign convention, while their flux, charge, flux-momentum, and charge-momentum are indicated by φ_M, q_M, ϱ_M, and σ_M, respectively. Moreover, the nonlinear characteristic functions of the phase-space models of FMR, CMR, FMC, CMMC, FMMI, and CMI, are denoted by Ψ^F_{mr}, Ψ^C_{mr}, Ψ^F_{mc}, Ψ^{CM}_{mc}, Ψ^{FM}_{mi}, and Ψ^C_{mi}, respectively. Using this notation, the phase-space models of the memelements assume the formulation reported in the second column of Table 1 (see [18,42]). It is known that the function Ψ of each memelement is the derivative of the function Φ which defines the constitutive relationship of the memelement itself, i.e.,

$$\Psi(x) = \frac{d}{dx}\Phi(x) \ . \tag{32}$$

The functions Φ pertaining to the mememelents are denoted as in the fifth column of Table 1. For the sake

Table 1 Phase-space and input-output models of the six memelements. The terms $\mathcal{D}_{[t_0]}^{-2} i_M$ and $\mathcal{D}_{[t_0]}^{-2} v_M$ represent the functions obtained via the double integrals $\int_{t_0}^{t} \left(\int_{t_0}^{\tau} i_M(\eta) d\eta \right) d\tau$ and $\int_{t_0}^{t} \left(\int_{t_0}^{\tau} v_M(\eta) d\eta \right) d\tau$, respectively

Memelement (Code)	Phase-Space model	Input-Output model	Ψ	Φ
FMR: flux-controlled memristor	$\begin{cases} \mathcal{D}\varphi_M = v_M \\ i_M = \Psi(\varphi_M) v_M \end{cases}$	$i_M = \mathcal{D}\Phi\left(\mathcal{D}_{[t_0]}^{-1} v_M\right)$	Ψ_{mr}^{F}	Φ_{mr}^{F}
CMR: charge-controlled memristor	$\begin{cases} \mathcal{D}q_M = i_M \\ v_M = \Psi(q_M) i_M \end{cases}$	$v_M = \mathcal{D}\Phi\left(\mathcal{D}_{[t_0]}^{-1} i_M\right)$	Ψ_{mr}^{C}	Φ_{mr}^{C}
FMC: flux-controlled memcapacitor	$\begin{cases} \mathcal{D}\varphi_M = v_M \\ q_M = \Psi(\varphi) v_M \\ i_M = \mathcal{D}q_M \end{cases}$	$i_M = \mathcal{D}^2\Phi\left(\mathcal{D}_{[t_0]}^{-1} v_M\right)$	Ψ_{mc}^{F}	Φ_{mc}^{F}
CMMC: charge momentum-controlled memcapacitor	$\begin{cases} \mathcal{D}q_M = i_M \\ \mathcal{D}\sigma_M = q_M \\ v_M = \Psi(\sigma_M) q_M \end{cases}$	$v_M = \mathcal{D}\Phi\left(\mathcal{D}_{[t_0]}^{-2} i_M\right)$	Ψ_{mc}^{CM}	Φ_{mc}^{CM}
CMI: charge-controlled meminductor	$\begin{cases} \mathcal{D}q_M = i_M \\ \varphi_M = \Psi(q_M) i_M \\ v_M = \mathcal{D}\varphi_M \end{cases}$	$v_M = \mathcal{D}^2\Phi\left(\mathcal{D}_{[t_0]}^{-1} i_M\right)$	Ψ_{mi}^{C}	Φ_{mi}^{C}
FMMI: flux momentum-controlled meminductor	$\begin{cases} \mathcal{D}\varphi_M = v_M \\ \mathcal{D}\varrho_M = \varphi_M \\ i_M = \Psi(\varrho_M) \varphi_M \end{cases}$	$i_M = \mathcal{D}\Phi\left(\mathcal{D}_{[t_0]}^{-2} v_M\right)$	Ψ_{mi}^{FM}	Φ_{mi}^{FM}

of the simplicity, we enforce the following hypothesis on Φ.

Assumption 1 The constitutive relation of each memelement is defined by a nonlinear function $\Phi(x) : \mathbb{R} \to \mathbb{R}$ of class $\mathcal{C}^i(\mathbb{R})$, $i \geq 1$, and such that $\Phi(0) = 0$.

Assumption 1 has an important consequence in modeling the memelements. Indeed, if the characteristic function Ψ of a memelement has as argument the function of time x, then, assuming this latter differentiable, the function Φ satisfies

$$\mathcal{D}\Phi\big(x(t)\big) = \Psi\big(x(t)\big) \cdot \mathcal{D}x(t) \tag{33}$$

Exploiting property (33) in the memelement phase-space models directly brings to the input-output formulations reported in the third column of Table 1.

Since the interconnection of Σ_L with the ideal memelement is described by the following equations:

$$\begin{cases} v_M = v_L \\ i_M = -i_L \end{cases}, \tag{34}$$

we can readily derive the input-output model of the CT memristive circuit. To this aim, notice that the equations in the third column of Table 1 are well suited for substituting the electric variables at their left hand side directly into the input-output models of Σ_L. Therefore, for building the model of the CT circuit we employ the following scheme.

- FMR, FMC, and FMMI are connected to the impedance input-output model of Σ_L.
- CMR, CMMC, and CMI are connected to the admittance input-output model of Σ_L.

The six circuit models coming up from the above scheme and configuration (34) can be conveniently framed into a general formulation by introducing the following notation. First, observe that all the input-output models of the memelements can be written in the form

$$y = \mathcal{D}^{\beta+1}\Phi\left(\mathcal{D}_{[t_0]}^{-(\alpha+1)} z\right) \tag{35}$$

where y, z, Φ, α, and β are as in Table 2. Then, the compatible input-output model of Σ_L can be represented as

$$z = -M(\mathcal{D}) y \tag{36}$$

where again y, z, and $M(\mathcal{D})$ are as reported in Table 2. Therefore, substituting y from (35) into (36) brings to

$$z + M(\mathcal{D})\mathcal{D}^{\beta+1}\Phi\left(\mathcal{D}_{[t_0]}^{-(\alpha+1)} z\right) = 0 \tag{37}$$

Table 2 Keys for the interpretation of equations (35), (37), and (39)

Memelement code	x	y	z	Ψ	Φ	$M(\mathcal{D})$	$P(\mathcal{D})$	$Q(\mathcal{D})$	α	β
FMR	φ_M	i_M	v_M	Ψ_{mr}^F	Φ_{mr}^F	$L(\mathcal{D})$	$R(\mathcal{D})$	$S(\mathcal{D})$	0	0
CMR	q_M	v_M	i_M	Ψ_{mr}^C	Φ_{mr}^C	$\bar{L}(\mathcal{D})$	$S(\mathcal{D})$	$R(\mathcal{D})$	0	0
FMC	φ_M	i_M	v_M	Ψ_{mc}^F	Φ_{mc}^F	$L(\mathcal{D})$	$R(\mathcal{D})$	$S(\mathcal{D})$	0	1
CMMC	σ_M	v_M	i_M	Ψ_{mc}^{CM}	Φ_{mc}^{CM}	$\bar{L}(\mathcal{D})$	$S(\mathcal{D})$	$R(\mathcal{D})$	1	0
CMI	q_M	v_M	i_M	Ψ_{mi}^C	Φ_{mi}^C	$\bar{L}(\mathcal{D})$	$S(\mathcal{D})$	$R(\mathcal{D})$	0	1
FMMI	ϱ_M	i_M	v_M	Ψ_{mi}^{FM}	Φ_{mi}^{FM}	$L(\mathcal{D})$	$R(\mathcal{D})$	$S(\mathcal{D})$	1	0

Then, observe that from the phase-space models in the first column of Table 1 it follows that

$$z = \mathcal{D}^{\alpha+1} x \tag{38}$$

where as before x, z, and α are the ones reported in Table 2. Hence, substituting (38) into (37) provides the final form of the complete circuit model:

$$\mathcal{D}^{\alpha+1} x + M(\mathcal{D}) \mathcal{D}^{\beta+1} \Phi(x) = 0 \tag{39}$$

Notice that the rational function $M(\mathcal{D})$ can be also written as

$$M(\mathcal{D}) = \frac{Q(\mathcal{D})}{P(\mathcal{D})} \tag{40}$$

where the polynomial P and Q depends on those in (29) according to the relationships reported in Table 2. Therefore, the solvability of equation (39) requires that Φ is sufficiently differentiable.

Proposition 1 *Consider the CT circuit of Fig. 1 where the linear two-terminal element Σ_L obeys a differential equation of the form (29) and is connected to the ideal memelement according to (34). Then, if Assumption 1 holds with $i = order[\mathcal{D}^{\beta+1} Q(\mathcal{D})]$, then the circuit is described by the nonlinear differential equation*

$$\mathcal{D}\left(\mathcal{D}^{\alpha} P(\mathcal{D}) x + \mathcal{D}^{\beta} Q(\mathcal{D}) \Phi(x)\right) = 0 \tag{41}$$

where x, Φ, P, Q, α, and β are as in Table 2.

Proof The result directly comes from the application of (40) into the formal representation (39), which brings to the actual differential equation model after noticing that $\mathcal{D}$ commutes with any polynomial operator such as $P(\mathcal{D})$ and $Q(\mathcal{D})$. □

Remark 1 If order$[\mathcal{D}^{\alpha} P(\mathcal{D})]$ > order$[\mathcal{D}^{\beta} Q(\mathcal{D})]$ the nonlinear differential equation (41) is explicit, a condition typically enforced when modeling CT memristive circuits (see [42] and references therein). From Table 2 it follows that the strict causality of $M(\mathcal{D})$, i.e., order$[P(\mathcal{D})]$ > order$[Q(\mathcal{D})]$, is required only in the case of FMR, CMR, FMC, and CMI. Furthermore, observe that the order of the differential equation is $1 + \alpha +$ order$[P(\mathcal{D})]$, thus it increases with the order of the impedance/admittance of Σ_L.

Corollary 2 *The nonlinear differential equation (41) has a first integral described by the relationship*

$$\mathcal{D}^{\alpha} P(\mathcal{D}) x + \mathcal{D}^{\beta} Q(\mathcal{D}) \Phi(x) = \mu \tag{42}$$

for any $\mu \in \mathbb{R}$ such that (42) admits a solution.

Proof The constant relationship (42) is a direct consequence of removing $\mathcal{D}$ in the nonlinear differential equation (41), since any solution $x(t)$ of (41) should be such that the function of time $\mathcal{D}^{\alpha} P(\mathcal{D}) x(t) + \mathcal{D}^{\beta} Q(\mathcal{D}) \Phi(x(t))$ is constant over time t. Then, the existence of the first integral depends only on the solvability of the nonlinear differential equation (42), that is guaranteed by Assumption 1 with $i = \text{order}[\mathcal{D}^{\beta+1} Q(\mathcal{D})]$. This also implies the existence of at least one proper value of μ. Anyways, the actual values of μ for which equation (42) admits solutions, depend on the problem configuration. □

Remark 2 As already pointed out for the circuit in Section 3, (42) describes the *foliation feature* of the phase space of the CT circuits in Fig. 1: each value of the index μ, that makes equation (42) solvable, defines an invariant manifold in the phase-space of the circuit. By varying the index μ we get a continuum of invariant manifolds which covers the entire phase-space (see also [17]).

Table 3 Discretization operators based on numerical integration techniques

Method	Discretization Operator	
Forward Euler method	$\Delta(T, h_T) = \frac{h_T - 1}{T}$	(43)
Backward Euler Method	$\Delta(T, h_T) = \frac{h_T - 1}{T h_T}$	(44)
Theta method	$\Delta(T, h_T) = \frac{1}{T} \frac{h_T - 1}{(1-\theta)h_T + \theta}$ $\theta \in [0, 1]$	(45)
Midpoint Rule or Modified Euler method	$\Delta(T, h_T) = \frac{h_T - h_T^{-1}}{2T} = \frac{h_T^2 - 1}{2T h_T}$	(46)
Tustin Method or Trapezoidal rule	$\Delta(T, h_T) = \frac{2}{T} \frac{h_T - 1}{h_T + 1}$	(47)

5 Main result

In this section we illustrate a discretization technique of CT memristive circuit of Fig. 1, which generates DT maps preserving the first integral feature and the related foliation of the phase-space into a continuum of invariant manifolds.

5.1 A discretization procedure for CT memristive circuits

Let us now formalize the procedure already used in Section 3 to derive the DT maps from the CT circuit. First of all, observe that a generic discretization operator may not be able, in general, to preserve the structural properties of a CT system, as already shown in Section 3. Indeed, a first integral is a fragile property and it can be destroyed even for arbitrarily small T. Therefore, we introduce the following assumptions to select a particular, though very broad, class of the discretization operators introduced in Definition 3.

Assumption 2 The discretization operator $\Delta(T, h_T)$ is a rational function of h_T, i.e.,

$$\Delta(T, h_T) = \frac{V_T(h_T)}{W_T(h_T)} \tag{48}$$

where V_T and W_T are two polynomials, whose coefficients are polynomials of T.

Assuming that $\mathcal{D} f(t) = g(t)$ and according to Definition 3, it follows that

$$\lim_{T \to 0^+} \left(\frac{V_T(h_T)}{W_T(h_T)} f(t) - g(t) \right) = 0 \tag{49}$$

which implies that the time-derivative of f at time t can be written as

$$\mathcal{D} f(t) = \frac{V_T(h_T)}{W_T(h_T)} f(t) + o\left(T^\eta\right) \tag{50}$$

where $\eta \geq 1$ depends on the power development with respect to T of $V_T(h_T) f(t)$ and $W_T(h_T) g(t)$ around t.

Assumption 3 For any constant function $f(t) = \mu \in \mathbb{R}, \forall t \in \mathbb{R}$, the discretization operator $\Delta(T, h_T)$ is such that

$$\Delta(T, h_T) f(t) = \Delta(T, h_T)\mu = 0 \,, \quad \forall T > 0.$$

Notice that this assumption implies that $V_T(h_T)$ in (48) must have the factor $h_T - 1$, i.e., $V_T(1) = 0$ and $W_T(1) \neq 0$.

The following result is used to derive and characterize the sought DT maps for the class of CT memristive circuits defined by Proposition 1.

Proposition 3 *Consider the CT circuit of Fig. 1 and assume that Proposition 1 holds. Choose a discretization operator $\Delta(T, h_T)$ which satisfies Assumption 2 and substitute $\mathcal{D} \leftarrow \Delta(T, h_T)$ into the differential equation (41). Moreover, consider the relationship obtained neglecting the residual little-o term, i.e.,*

$$\Delta(T, h_T)\Big(\Delta(T, h_T)^\alpha P(\Delta(T, h_T)) x_d + \Delta(T, h_T)^\beta Q(\Delta(T, h_T)) \Phi(x_d) \Big) = 0 \,, \tag{51}$$

and denote its solution as $x_d(t)$. Finally, define $x_k = x_d(t)|_{t=kT} = x_d(kT)$, $k \in \mathbb{Z}$, and substitute $h_T \leftarrow h$ in (51). Then, the result is a DT map described by a difference equation of the form

$$F_T\big(x_{k+n},\dots,x_k\big)+G_T\big(\Phi(x_{k+m}),\dots,\Phi(x_k)\big)=0 \tag{52}$$

where m and n are positive integers, and F_T and G_T are T-parametric linear functions in their arguments.

Proof Because of Assumption 2, $\Delta(T,h_T)$ has the form (48) of a T-parametric rational function in h_T for two polynomial functions V_T and W_T. Then, if we substitute in (41) the expression (50) of $\mathcal{D}$ in terms of $\Delta(T,h_T)$, the complete circuit dynamics boils down to

$$\underbrace{\frac{V_T^{\alpha+1}(h_T)}{W_T^{\alpha+1}(h_T)}P\left(\frac{V_T(h_T)}{W_T(h_T)}\right)}_{[\triangle]}x + \underbrace{\frac{V_T^{\beta+1}(h_T)}{W_T^{\beta+1}(h_T)}Q\left(\frac{V_T(h_T)}{W_T(h_T)}\right)}_{[\triangledown]}\Phi(x)=o\left(T^{\nu}\right) \tag{53}$$

where the little-o term $o\left(T^{\nu}\right)$ collects all the residuals from (50), and its order $\nu\in\mathbb{Z}_+$ depends on the form of $\Delta(T,h_T)$, P and Q. Observe that the terms $[\triangle]$ and $[\triangledown]$ are rational functions in h_T. Therefore, computing and removing the maximum common divisor leads to an equation of the form

$$F_T\big(h_T^n,\dots,h_T^1,h_T^0\big)x + G_T\big(h_T^m,\dots,h_T^1,h_T^0\big)\Phi(x)=o\left(T^{\omega}\right)$$

where F_T and G_T are T-parametric polynomial functions of h_T. The maximum orders m and n of the powers of h_T depends on order[P], order[Q], α, and β, while ω depends on ν and the power development of the maximum common divisor. Notice that the corresponding operators $F_T\big(h_T^n,\dots,h_T^1,h_T^0\big)$ and $G_T\big(h_T^m,\dots,h_T^1,h_T^0\big)$ can be applied to x and $\Phi(x)$, respectively, thus obtaining

$$F_T\big(h_T^n x(t),\dots,h_T x(t),x(t)\big) + G_T\Big(h_T^m\Phi\big(x(t)\big),\dots,h_T\Phi\big(x(t)\big),\Phi\big(x(t)\big)\Big) = o\left(T^{\omega}\right)\,.$$

Now, neglecting the residual term yields the following equation

$$F_T\big(h_T^n x_d(t),\dots,h_T x_d(t),x_d(t)\big) + G_T\Big(h_T^m\Phi\big(x_d(t)\big),\dots,h_T\Phi\big(x_d(t)\big),\Phi\big(x_d(t)\big)\Big)=0\,, \tag{54}$$

whose solution has been denoted as $x_d(t)$. Then, letting $t=kT$ and substituting h_T with h, equation (54) becomes

$$F_T\big(h^n x_d(kT),\dots,hx_d(kT),x_d(kT)\big) + G_T\Big(h^m\Phi\big(x_d(kT)\big),\dots,h\Phi\big(x_d(kT)\big),\Phi\big(x_d(kT)\big)\Big) = 0\,,$$

which provides the sought DT map in the form (52), since $x_k = x_d(kT)$, $h^i x_d(kT) = x_{k+i}$, and $h^i\Phi(x_d(kT))=\Phi(x_{k+i})$. □

Remark 3 Proposition 3 holds for any $T>0$ and any operator $\Delta(T,h_T)$ satisfying Assumption 2. However, note that the DT map (52) is explicit only if $n>m$. Nonetheless, it can be checked that, when the differential equation (41) is explicit, i.e. when order$[\mathcal{D}^{\alpha}P(\mathcal{D})]>$ order$[\mathcal{D}^{\beta}Q(\mathcal{D})]$, the orders of the T-parametric polynomial functions F_T and G_T in (52) satisfy $n>m$ if and only if order$[V_T(h_T)]>$ order$[W_T(h_T)]$. Furthermore, observe that the order n of the explicit DT map (52) is not less of the order $1+\alpha+$ order$[P(\mathcal{D})]$ of the nonlinear differential equation (41) and it increases with order$[V_T(h_T)]$. Hence, if the order of the discretization operator and the impedance/admittance of Σ_L (see Remark 1) are high, then the DT map may require particular attention from a computational point of view.

The next result proves that the discretization procedure in Proposition 3 preserves the *foliation feature* of the CT memristive circuits.

Theorem 4 *Under the hypothesis of Assumption 3 the DT map (52) of Proposition 3 evolves on invariant manifolds described by the relationship*

$$\Delta_T(h)^{\alpha}P\big(\Delta_T(h)\big)x_k+\Delta_T(h)^{\beta}Q\big(\Delta_T(h)\big)\Phi(x_k)=\bar{\mu}, \tag{55}$$

where $\bar{\mu} \in \mathbb{R}$ is a constant.

Proof Consider the discretization procedure used in the proof of Proposition 3, i.e substitute $\mathcal{D} \leftarrow \Delta(T, h_T)$ in equation (41), neglect the residual term to get equation (51), and then, letting $t = kT$ and $x_k = x_d(kT)$, $k \in \mathbb{Z}_+$, substitute $h_T \leftarrow h$. This way we get the following formal equation describing the DT map (52) of Proposition 3

$$\Delta_T(h) \times \underbrace{\Big(\Delta_T(h)^\alpha P\big(\Delta_T(h)\big)x_k + \Delta_T(h)^\beta Q\big(\Delta_T(h)\big)\Phi(x_k)\Big)}_{[\diamond]} = 0\,. \tag{56}$$

Since Assumption 3 ensures that $\Delta_T(h)$ has the factor $h-1$ at the numerator, we have the term $[\diamond]$ in (56) is constant over time, thus concluding the proof. □

Remark 4 Observe that relationship (55) describes an invariant manifold for the dynamics of the DT system (56). Indeed, the entire sequence $\{x_k\}_{k\in\mathbb{Z}}$ satisfies (55) for the same $\bar{\mu}$. Therefore, the discretization procedure of Proposition 3 preserves, for any time step $T > 0$, the foliation feature of the memristive circuit (41) in the phase-space defined by x_k and the finite number of its ahead shifted values x_{k+i} involved in (55). In this perspective, the constant $\bar{\mu}$ in (55) acts as the index of the invariant manifold, as well as μ is the index of the CT first integral.

Observe that, thanks to property (6), equation (51) tends to the same form of equation (41) as $T \to 0^+$. Hence, it is expected that the solution of equation (51), here denoted by $x_d(t, T)$ to make explicit its dependence on T, is a local approximation of the solution $x(t)$ of (41), with increasing precision as $T \to 0^+$. Clearly, to ensure such a result it is necessary that the starting configuration of $x_d(t, T)$ converges to that of $x(t)$ as $T \to 0^+$. To this regard, observe that the initial conditions at t_0 of $x(t)$ are given in the form $\mathcal{D}^i x(t_0)$, $i = 0, 1, \ldots$, because model (41) is a differential equation. Conversely, the initial conditions of $x_d(t, T)$ are given as $x_d(t_0 - jT, T)$, $j = 0, 1, \ldots$, because model (51) is a formal way to denote the delayed equation (54). Nonetheless, the starting configuration of $x_d(t, T)$ can be converted into the initial conditions of $\Delta^i(T, h_T)x(t_0)$, $i = 0, 1, \ldots$, that by construction converge to $\mathcal{D}^i x(t_0)$ as $T \to 0^+$. Hence, for any fixed $t \geq t_0$ the function $x_d(t, T)$ actually tends to $x(t)$ and in this sense it behaves as its local approximation. This reasoning is summarized in the next result.

Corollary 5 *Assume that $x(t)$ is the solution of (41) for $t \geq t_0$, and that the initialization at t_0 of system (51) converges to the starting configuration of (41) as $T \to 0^+$. Then, for each fixed instant $t \geq t_0$*

$$\lim_{T\to 0^+} x_d(t, T) = x(t)\,. \tag{57}$$

Remark 5 The meaning of Corollary 5 is that, for sufficiently small T, the solution x_k of the map (52) can be regarded as an approximation of the solution $x(t)$ of (41) for $t = kT$. Nonetheless, since (57) ensures a point-wise convergence with respect to a fixed k, no general conclusions can be drawn on the behavior of the difference $x(kT) - x_k$ for large values of k.

Finally, we stress that Proposition 3 is related to the problem of the numerical simulation of a CT system, but it is conceptually different. Indeed, the goal of simulation is to generate a DT sequence that always stays close to the original CT solution. To this aim, it uses not only a DT map approximating the CT system, but also a variety of tools able to limit the propagation error and to avoid that the CT and DT solutions may diverge beyond a certain threshold [44,45]. Instead, the discretization procedure outlined in Proposition 3 generates DT maps by simply substituting the derivative operator $\mathcal{D}$ with the DT operator $\Delta_T(h)$, without providing any specific tools for containing the propagation error. Rather, its main goal is to preserve the important foliation feature of the CT memristive circuits for any time step $T > 0$, as ensured by Proposition 4, leaving any issue regarding the propagation error only to the choice of a proper T, according to Corollary 5.

5.2 Discretization operators based on numerical integration

The discretization operators which satisfy Assumptions 2 and 3 are a very broad class. In the Appendix A.1, we will illustrate how the operators $\Delta(T, h_T)$ can be derived from the standard numerical integration techniques used for the simulation of CT systems, which indeed is a strictly related problem, as already underlined. The validity of the approach is general, but

its application to some particularly relevant and well-known techniques is briefly summarized in Table 3, while their derivation is postponed in Appendix A.1.

5.3 Discretization operators based on other techniques

Deriving the discretization operators from standard integration techniques is a simple, quick, and safe way to design approximations of $\mathcal{D}$ suited to implement the results of Proposition 3 and Theorem 4. Nevertheless, it is not the unique approach. Hereafter, for the sake of completeness, we briefly introduce a list of some alternative approaches which only require that $T > 0$ and the two functions $f(t) : \mathbb{R} \to \mathbb{R}$ and $g(t) : \mathbb{R} \to \mathbb{R}$ satisfy (1), i.e., $g(t) = \mathcal{D}f(t)$.

- **Single-stage multi-step methods.** The basic idea of these techniques is to approximate the integral function f with a properly chosen substitute obtained interpolating over several steps ("multi-step") of the same amplitude T ("single-stage"). The interpolation points have the form $\big(t + jT, f(t + jT)\big)$, for a finite set J of chosen integer values of j, i.e., $j \in J \subset \mathbb{Z}$. The interpolating function is then analytically derived at time t, and its derivative, that depends on the interpolation points, gives the discretization operator by replacing each $f(t + jT)$ first with $h_T^j f(t)$ and then with the discrete variable $h^j f_k$, where $f_k = f(kT)$. More details on these techniques are in Appendix A.2.
- **Multi-stage single-step methods.** These techniques are based on local interpolation problems applied to the function g, that is approximated over $[t, t+T]$ ("single-step"), using for refinement a number of additional intermediate points taken in the same interval ("multi-stage"). The interpolation points have the form $\big(t + jT, g(t + jT)\big)$, for a finite set J of chosen real values of $j \in J \subset [0, 1] \subset \mathbb{R}$. The interpolating function is then analytically integrated to get the inverse of a discretization operator. More details on these techniques are in Appendix A.3.
- **Averaging methods.** These techniques perform a weighted mean among chosen discretization operators, mixing their features. If the starting operators already satisfy both Assumptions 2 and 3, then the same does the obtained final operator. More details on these techniques are in Appendix A.4.

6 Application example

Consider the CT memristive circuit of Fig. 2, where the two-terminal element Σ_L is the same of the circuit in Section 3, while the flux-controlled memristor has been replaced with a meminductor controlled by the flux-momentum ϱ_M, whose phase-space model is as in Table 1. The application of Proposition 1 yields that the dynamics of the circuit obeys

$$\mathcal{D}\left(\left(\mathcal{D} + \frac{1}{RC}\right)\mathcal{D}\varrho_M + \frac{1}{C}\Phi_{mi}^{FM}(\varrho_M)\right) = 0\,. \tag{58}$$

Assuming that

$$\Phi_{mi}^{FM}(\varrho) = \gamma_1\varrho + \gamma_2\varrho^2 + \gamma_1\varrho^3\,,$$

from Corollary 2 we get that the first integrals are defined by the following equation:

$$\left(\mathcal{D} + \frac{1}{RC}\right)\mathcal{D}\varrho + \frac{1}{C}\left(\gamma_1\varrho + \gamma_2\varrho^2 + \gamma_3\varrho^3\right) = \mu\,. \tag{59}$$

Figure 6 illustrates the foliation of the phase-space of system (58) using the following configuration in normalized units of measure:

$$R = 1 \quad C = 1 \quad \gamma_1 = -10 \quad \gamma_2 = 0 \quad \gamma_3 = 1.$$

Apply now Proposition 3 to build a DT map using the Forward Euler discretization operator (43) in Table 3. We obtain the map:

$$\frac{h-1}{T}\underbrace{\left(\frac{h^2-2h+1}{T^2}\varrho_k + \frac{1}{RC}\frac{h-1}{T}\varrho_k + \frac{\gamma_1}{C}\varrho_k + \frac{\gamma_2}{C}\varrho_k^2 + \frac{\gamma_3}{C}\varrho_k^3\right)}_{[\oplus]} = 0$$

and equating the term $[\oplus]$ to $\bar{\mu}$ we get, according to equation (55) of Theorem 4, the equation of the DT invariant manifolds in the phase-space defined by ρ_k, ρ_{k+1}, and ρ_{k+2}. Straightforward computations lead to the explicit form of the map:

$$\varrho_{k+1} = \left(3 - \frac{T}{RC}\right)\varrho_k + \left(-3 + \frac{2T}{RC} - \frac{\gamma_1 T^2}{C}\right)\varrho_{k-1}$$

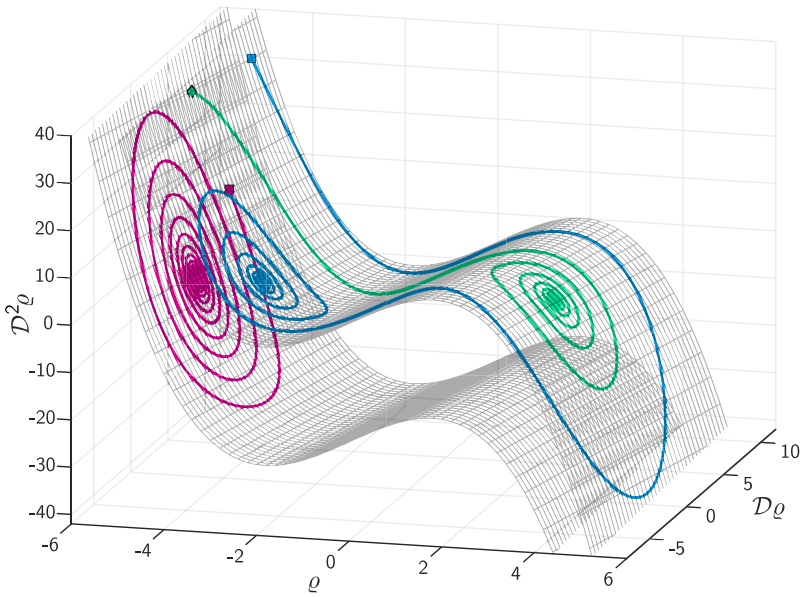

Fig. 6 The grids depict two invariant manifolds of system (58) in the space of the phase-variables ϱ, $\mathcal{D}\varrho$, $\mathcal{D}^2\varrho$. The green and blue trajectories lie on the same manifold, and they converge to two different attractive points. The red trajectory corresponds to a different first integral

$$+\left(1-\frac{T}{RC}+\frac{\gamma_1 T^2}{C}\right)\varrho_{k-2} - \frac{\gamma_2 T^2}{C}\varrho_{k-1}^2-\frac{\gamma_3 T^2}{C}\varrho_{k-1}^3 + \frac{\gamma_2 T^2}{C}\varrho_{k-2}^2+\frac{\gamma_3 T^2}{C}\varrho_{k-2}^3 \tag{60}$$

Map (60) preserves the foliation property, i.e., its solutions evolves on invariant manifolds, as it happens for the CT memristive circuit. From Corollary 5 it is known that for sufficiently small values of T the map (60) locally approximates the trajectories of the memristive circuit. Nonetheless, the evolution of the approximation error depends on several factors and the effect of T on the DT dynamics may be unpredictable, as it will be discussed in Section 7.

The evolution of the green trajectory of Fig. 6 is depicted in Fig. 7 against sequences $\{\varrho_k\}$ generated by the map (60) for different values of T, but initialized at the same corresponding point of the CT solution. In Fig. 8 the sequences corresponding to the green and magenta trajectories of Fig. 6 have been drawn over their originals for a direct comparison that highlights how the discretization procedure preserves the structure of invariant manifolds.

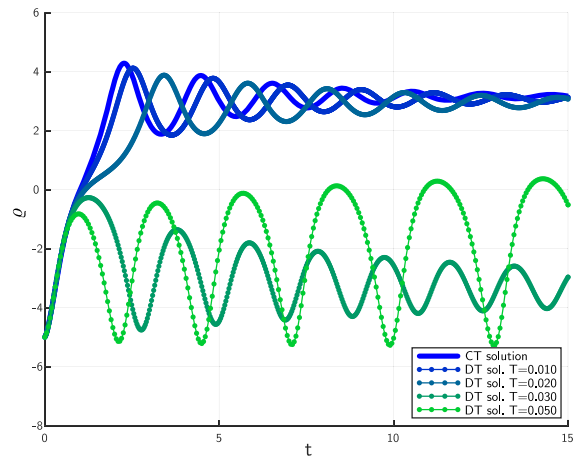

Fig. 7 Comparison between the CT trajectory of (58) and the corresponding DT solution of (60) for different values of T. For increasing values of T the propagation error between the two dynamics becomes larger. Over a certain threshold the DT solutions largely deviate from the CT one

7 Dependence of the DT maps on time step T

The discretization procedure of Section 5 generates DT maps which preserve the foliation feature of phase-space of the CT memristive circuit for any time step $T > 0$ and any discretization operator $\Delta(T, h_T)$ satisfying Assumptions 2 and 3.

Moreover, Corollary 5 has clarified that the solution x_k of the DT map derived via Proposition 3 provides a better approximation of the solution $x(t)$ at $t = kT$ of the CT circuit (41) when T is sufficiently small, as seen in the examples of Sections 3 and 6. Indeed, the most popular numerical integration meth-

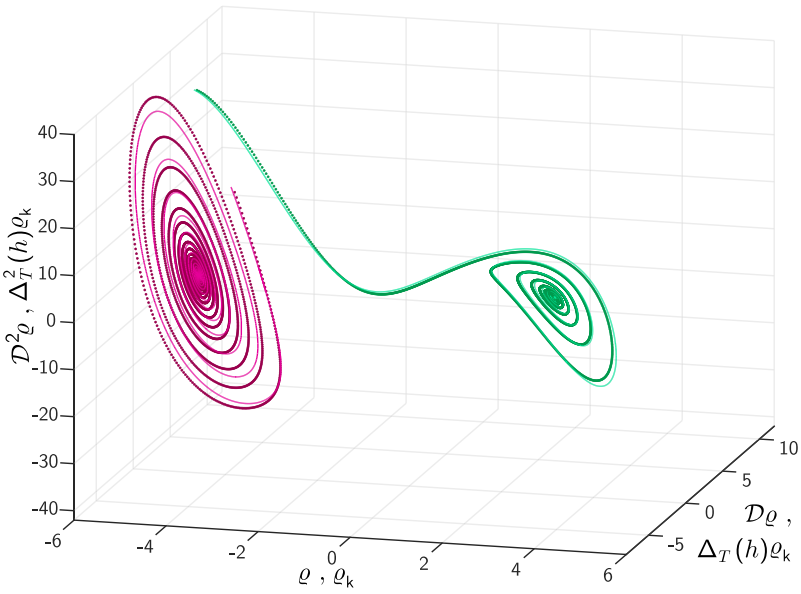

Fig. 8 The DT sequences obtained for $T = 0.005$ and initialized at the magenta square and green diamond of Fig. 6 are drawn over their CT counterparts. Even if the propagation error prevents the DT solutions to perfectly copy the CT trajectories, they remain sufficiently close to retain the same qualitative behaviour. The dependence of the green solutions on T is depicted in Fig. 7

ods implement adaptive mechanisms to dynamically adjust step T in order to ensure that x_k remains close to $x(kT)$ for large k [44,45].

If T is not sufficiently small then the DT map can exhibit dynamical behaviors completely different from those of the CT memristive circuit. Indeed, Edward N. Lorenz in [43] observed that, when one seeks approximate solutions of a set of differential equations by stepwise numerical integration, the choice of a not sufficiently small T may yield chaotic solutions, even if the true solutions approach limit cycles or equilibrium points. Such a phenomenon is known as computational chaos.

7.1 Embedding the logistic map in an RC-memristive circuit

Consider the RC-memristive circuit of Fig. 2 with a flux-controlled memristor as in Section 3. The circuit is described by the nonlinear differential equation (14) with Φ as in (17). Discretizing it via the Forward Euler Method leads to

$$\frac{h-1}{T}\underbrace{\left(\left(\frac{h-1}{T}+\frac{1}{RC}\right)\varphi_k+\frac{1}{C}\Phi(\varphi_k)\right)}_{[\otimes]}=0 \qquad (61)$$

and, according to Theorem 4, from $[\otimes]$ we get the DT invariant manifolds

$$\left(\frac{h-1}{T}+\frac{1}{RC}\right)\varphi_k+\frac{1}{C}\Phi(\varphi_k)=\bar{\mu}\ .$$

If the function Φ is chosen as in (17) with $\gamma_1 = 0$, $\gamma_2 = r/R$, $\gamma_3 = 0$, i.e.

$$\Phi(\varphi)=\frac{r}{R}\varphi^2\ , \qquad (62)$$

then the DT dynamics evolves on the invariant manifold of index $\bar{\mu}$ according to the equation

$$\varphi_{k+1}+\frac{T-RC}{RC}\varphi_k+\frac{rT}{RC}\varphi_k^2=\bar{\mu}T\ . \qquad (63)$$

Moreover, if time step T is chosen as

$$T=RC\ , \qquad (64)$$

then equation (63) becomes

$$\varphi_{k+1}+r\varphi_k^2=\bar{\mu}RC\ . \qquad (65)$$

Now, consider the logistic map [46]

$$y_{k+1}-ry_k+ry_k^2=0\ , \qquad (66)$$

where $r \in (0, 4)$. That map displays a chaotic attractor for $r \in (3.56995, 4)$. If we apply the change of

coordinate $y_k = z_k + \frac{1}{2}$, then (66) boils down to

$$z_{k+1} + r z_k^2 + \frac{1}{2}\left(1 - \frac{r}{2}\right) = 0\,. \tag{67}$$

A direct comparison between equations (65) and (67) reveals that, for each positive value of R and C, the discretized dynamics (63) of the RC-memristive circuit exhibits, under condition (64), a logistic map (67) onto its invariant manifolds. In particular, the index $\bar{\mu}$ of the DT invariant manifold where this happens is related to the parameter r of the logistic map as

$$\bar{\mu} = \underbrace{\frac{1}{2RC}\left(\frac{r}{2} - 1\right)}_{\bar{\mu}_0} \tag{68}$$

Moreover, relation (64) implies that for every chosen T there exists a circuit configuration of R and C, such that the logistic map is exhibited in the DT invariant manifold with the index $\bar{\mu} = \bar{\mu}_0$. Therefore, despite the CT circuit with Φ as in (62) is governed by the second-order dynamics (14) that is unable to exhibit complex behaviors, its DT counterpart (63) always has a manifold featuring a logistic map, that for proper values of r can display chaos.

The differential equation (14) describing the dynamics of the memristive circuit has been simulated with Φ as in (17) using the following configuration in normalized units of measure:

$$\begin{aligned} &R = 2\,, \quad C = 0.25\,, \quad r = 3.9\,, \\ &\gamma_1 = 0\,, \quad \gamma_2 = \frac{r}{R} = 1.95\,, \quad \gamma_3 = 0 \end{aligned} \tag{69}$$

Its foliated phase-space is depicted in Fig. 9, where two trajectories related to the same $\mu = 1.2$ have been highlighted. The evolution of the solution initialized at the diamond is reported in Fig. 10 against the DT sequences generated by (63) for different values of T. Observe that as T increases the DT sequence $\{\varphi_k\}$ separates itself from the CT solution $\varphi(t)$ and its behavior becomes very noisy.

Figure 11 illustrates the first-return maps of these DT sequences. They are compared with the first-return maps of the sampling $\varphi(kT)$ of the CT solution for the same values of T used in Fig. 10. For small T the first-return maps of both the sequences $\{\varphi_k\}$ and $\varphi(kT)$ are aligned along the straight line at 45°, because the related dynamics are slow with respect to T. However, as T increases they transform, and in particular the first-return map of the sequence $\{\varphi_k\}$ boils down to Fig. 11F when T satisfies (64).

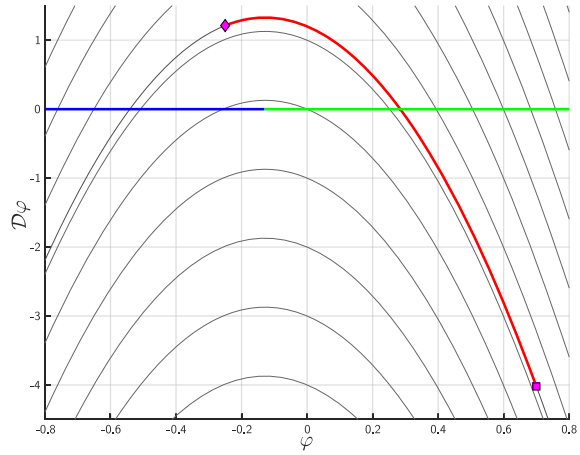

Fig. 9 Phase-space of system (14)-(17) under configuration (69). Grey: examples of the invariant manifolds. Green/blue: Stable and unstable fixed points along the manifolds. Red branch: It is covered by two different trajectories starting, respectively, at the diamond and square

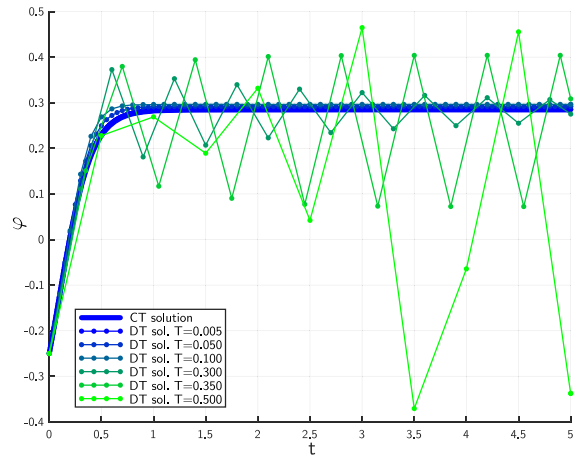

Fig. 10 Comparison between the CT trajectory of Fig. 9 starting at the red diamond and the DT solutions of (63) for different values of T. As T increases the accuracy of the DT map decreases, substantially diverging

A direct comparison with the first-return map of the logistic map (67), depicted in Fig. 12 for the same value of r in (69), reveals their strong relationship. Figure 13 illustrates the bifurcation diagram of (63) with respect to T. It highlights that the discretization step T plays the role of a bifurcation parameter lead-

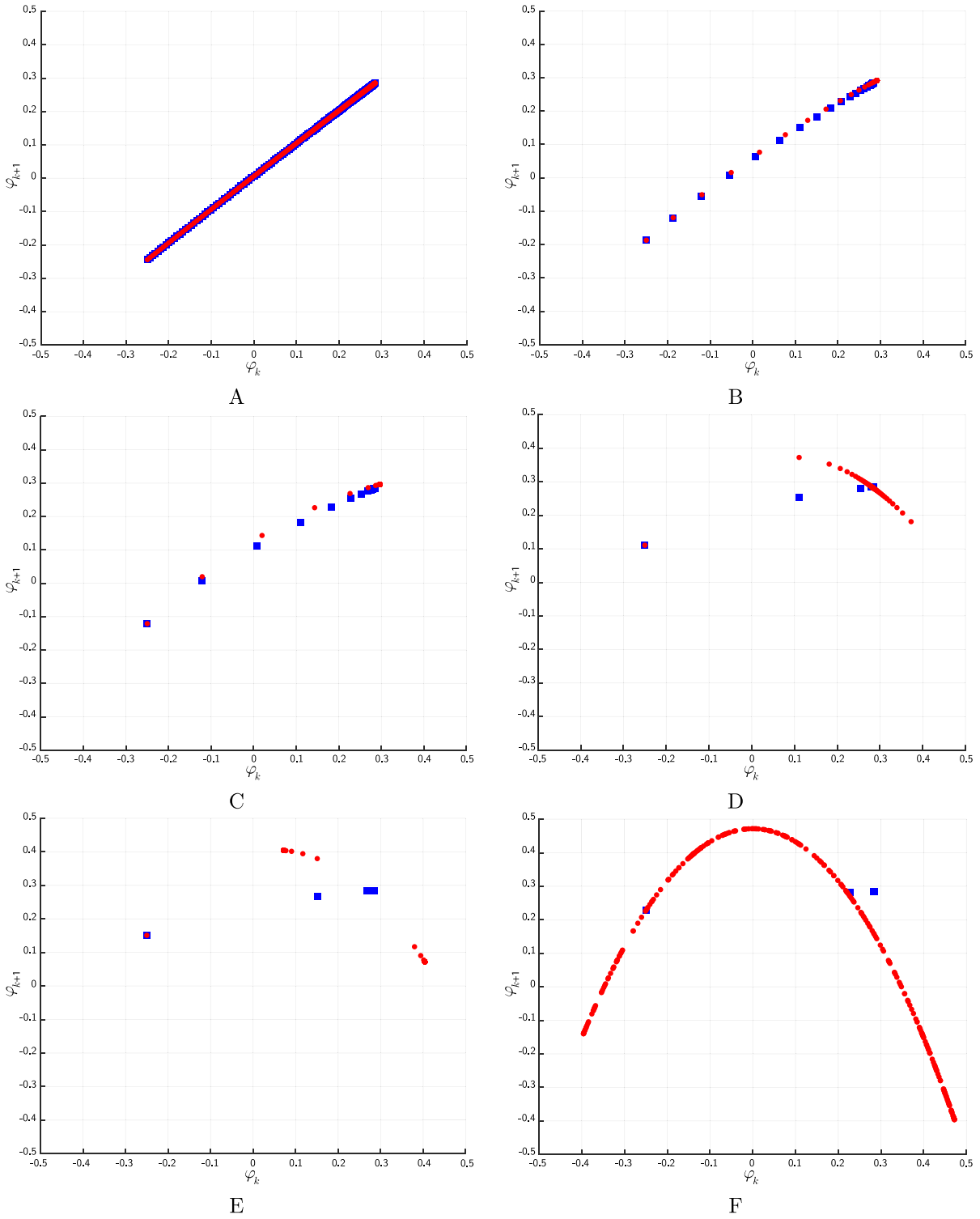

Fig. 11 First-return maps of the solutions illustrated in Fig. 10. Blue squares: First-return map of the CT trajectory sampled for different values of T. Red circles: First-return map of the DT solutions of (63) for the same values of T. A: $T = 0.005$. B: $T = 0.050$. C: $T = 0.100$. D: $T = 0.300$. E: $T = 0.350$. F: $T = 0.500$

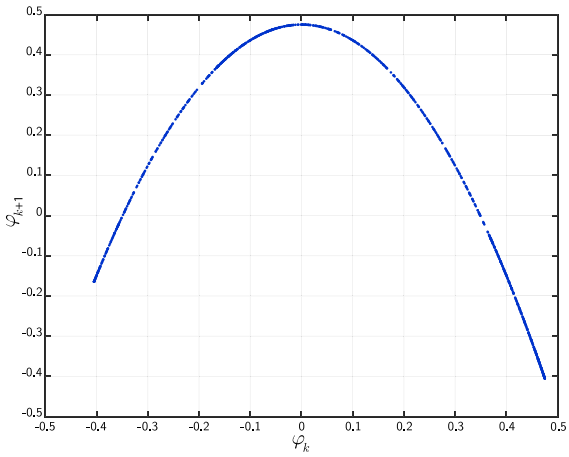

Fig. 12 The first-return map of the logistic equation (67). The comparison with the first-return map illustrated in Fig. 11F highlights their strong resemblance

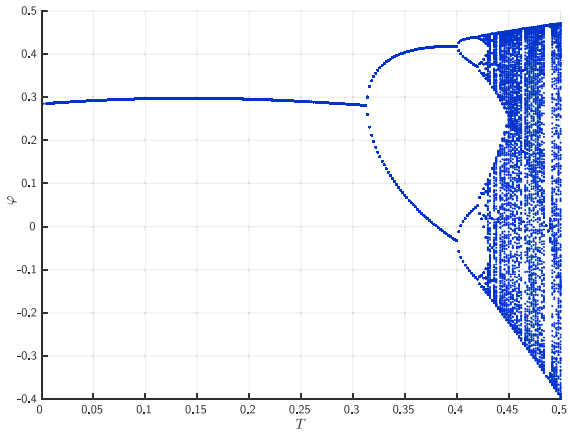

Fig. 13 Bifurcation diagram with respect to T of system (63). The blue dots are the peaks of the solution, that is initialized at $T = 0.005$ as in Fig. 10 and then followed by incrementing the bifurcation of small step up to $T = 0.500$

ing from DT maps providing a fair approximation of the CT one to the logistic map in a chaotic regime. Furthermore, it is worth recalling that the comparison between the samples $\varphi(kT)$ of the CT trajectory and the corresponding DT sequence $\{\varphi_k\}$ is meaningful only if they refer to the same behavior in the sense of Corollary 5, which states that their starting conditions must converge to the same initialization for $T \to 0^+$. The DT sequences $\{\varphi_k\}$ reported in Fig. 10 have been obtained by using the initial values $\varphi_0 = \varphi(0)$ and $\varphi_1 = \varphi(T)$, that indeed satisfy Corollary 5. However, that is not the only possible choice. For instance, another approach consists in choosing φ_0 and φ_1 so that $\varphi_0 = \varphi(0)$ and $(\varphi_1 - \varphi_0)/T = \mathcal{D}\varphi(0)$.

Finally, we investigate the dynamics occurring on the invariant manifolds close to the one with $\bar{\mu} = \bar{\mu}_0$. The goal is to verify if the chaotic behavior of the logistic map is robust, i.e. it persists also on nearby manifolds. Indeed, Fig. 14 shows that for $\bar{\mu} = \bar{\mu}_0 + \delta$, with $\delta \in \{0, -0.025, -0.050, -0.100\}$, the dynamics on the related manifolds still exhibits a chaotic behavior similar to that on the manifold of index $\bar{\mu} = \bar{\mu}_0$. This clearly shows the robustness of the chaotic attractor with respect to the invariant manifolds, thus highlighting that the DT map, obtained by discretizing the RC-memristive circuit of Fig. 2 with configuration (69) via the Forward Euler method with T as in (64), possesses infinitely many chaotic attractors, i.e., it displays extreme multistability.

To complete the discussion, we show that the dynamics on the invariant manifold with index $\bar{\mu} = \bar{\mu}_0 + \delta$, for small $|\delta|$, is indeed described by a logistic map of the form

$$x_{k+1} + (r+\varepsilon)x_k^2 + \frac{1}{2}\left(1 - \frac{r+\varepsilon}{2}\right) = 0\,, \tag{70}$$

which clearly displays a chaotic attractor if $r + \varepsilon \in [3.56995, 4.]$.
Indeed, if we let

$$x_k = \frac{r}{r+\varepsilon}\varphi_k \tag{71}$$

the map (70) becomes

$$\frac{r}{r+\varepsilon}\varphi_{k+1} + \frac{r^2}{r+\varepsilon}\varphi_k^2 + \frac{1}{2}\left(1 - \frac{r+\varepsilon}{2}\right) = 0\,,$$

which can be written equivalently as

$$\varphi_{k+1} + r\varphi_k^2 + \frac{r+\varepsilon}{2r}\left(1 - \frac{r+\varepsilon}{2}\right) = 0\,.$$

Hence, the logistic map (70) is equivalent to (67) on the manifold whose index $\bar{\mu} = \bar{\mu}_0 + \delta$ satisfies

$$(\bar{\mu}_0 + \delta)RC = \frac{r+\varepsilon}{2r}\left(\frac{r+\varepsilon}{2} - 1\right)\,,$$

which relates δ and ε as follows

$$\delta = \frac{\varepsilon}{2rRC}\left(2(r-1) + \varepsilon\right)\,. \tag{72}$$

Hence, we can conclude that by applying the proposed discretization procedure to the RC-memristive circuit

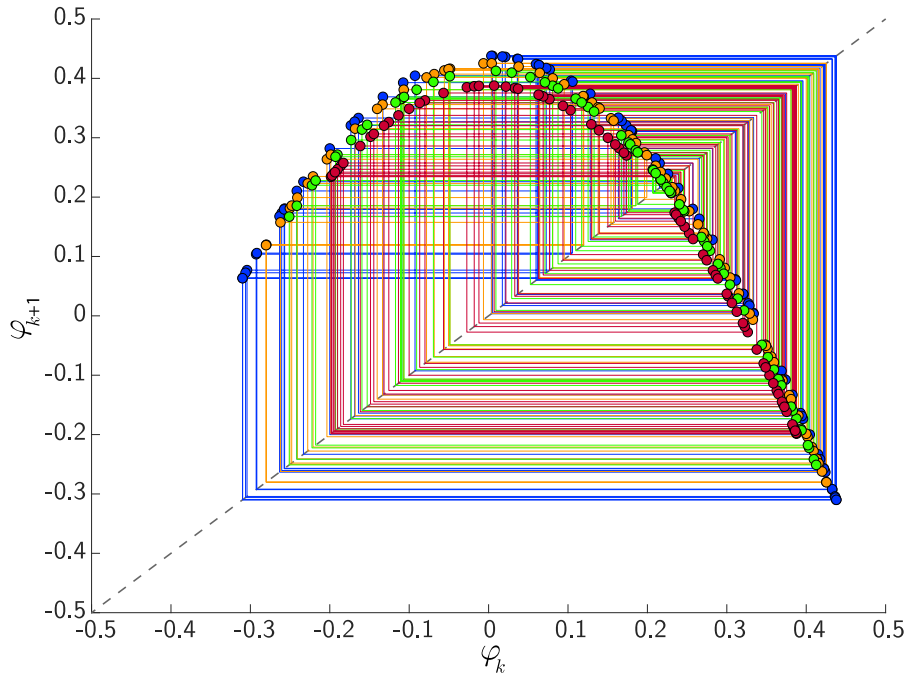

Fig. 14 Multiple chaotic attractors exhibited by the DT map (61) at $\bar{\mu} = \mu_0 + \delta$ for $\delta \in \{0, -0.025, -0.050, -0.100\}$. The evolution of the states is highlighted by linking the "dots" with solid lines intersecting the bisector (dashed line)

of Fig. 2 with configuration (69) via the Forward Euler method, we have derived a DT map that displays a chaotic attractor on each manifold such that $\bar{\mu} = 0.95 + \varepsilon\frac{5.8+\varepsilon}{3.9}$ with $\varepsilon \in (-0.33005, 0.1)$.

7.2 Embedding the Henon map in an RC-memristive circuit

Consider the same RC-memristive circuit of of Section 7.1, but now apply the discretization operator (A7) obtained by averaging the Forward and Backward Euler Methods. The corresponding DT map boils down to

$$\frac{\lambda h^2 + (1-2\lambda)h - (1-\lambda)}{Th} \times \underbrace{\left(\left(\frac{\lambda h^2 + (1-2\lambda)h - (1-\lambda)}{Th} + \frac{1}{RC}\right)\varphi_k + \frac{1}{C}\Phi(\varphi_k)\right)}_{[\odot]} = 0\,. \tag{73}$$

The term $[\odot]$ catches the existence of the DT invariant manifolds, where the trajectories follow the dynamics

$$\left(\frac{\lambda h^2 + (1-2\lambda)h - (1-\lambda)}{Th} + \frac{1}{RC}\right)\varphi_k + \frac{1}{C}\Phi(\varphi_k) = \bar{\mu}\,. \tag{74}$$

For $\lambda \neq 0$ map (74) admits the explicit form

$$\varphi_{k+1} + \frac{T + (1-2\lambda)RC}{\lambda RC}\varphi_k - \frac{1-\lambda}{\lambda}\varphi_{k-1} + \frac{T}{\lambda C}\Phi(\varphi_k) = \bar{\mu}\frac{T}{\lambda}\,. \tag{75}$$

Clearly, for $\lambda = 1$ this map boils down to the map (63) used in Section 7.1. Assume now Φ is chosen as in (17) with $\gamma_1 = 0$, $\gamma_2 = \frac{aC}{R(b-1)}$, and $\gamma_3 = 0$, i.e.

$$\Phi(\varphi) = \frac{aC}{R(b-1)}\varphi^2\,, \tag{76}$$

and let

$$\lambda = \frac{1}{b+1}. \tag{77}$$

Then, (75) boils down to

$$\varphi_{k+1} + \left(\frac{T}{RC}(b+1) + (b-1)\right)\varphi_k - b\varphi_{k-1} + \frac{aT(b+1)}{RC(b-1)}\varphi_k^2 = \bar{\mu}(b+1)T\,, \tag{78}$$

which, for every choice of $R > 0$ and $C > 0$, reduces to

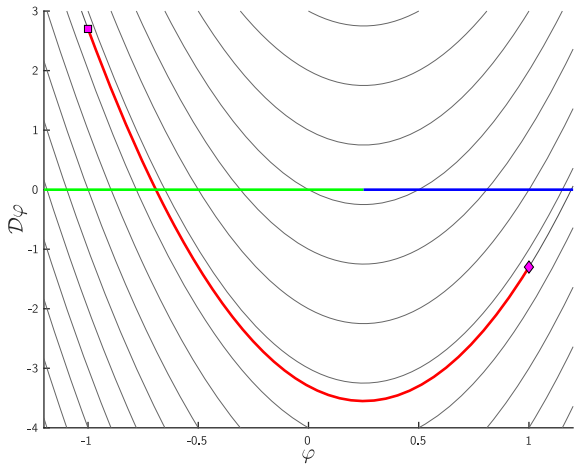

Fig. 15 Phase-space of system (14)-(17) under configuration (81). Grey: examples of the invariant manifolds. Green/blue: Stable and unstable fixed points along the manifolds. Red branch: It is covered by two different trajectories starting, respectively, at the diamond and square

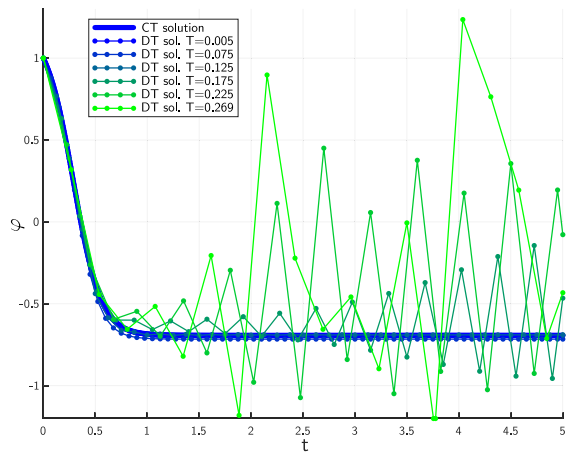

Fig. 16 Comparison between the CT trajectory of Fig. 9 starting at the red diamond and the DT solutions of (78) for different values of T. As T increases the accuracy of the DT map decreases, substantially diverging

$$\varphi_{k+1} - b\varphi_{k-1} - a\varphi_k^2 = \bar{\mu}(1-b)RC \,,$$

when

$$T = RC\frac{1-b}{b+1} \,. \tag{79}$$

A comparison with the input-output formulation of the Henon map [46]

$$y_{k+1} - by_{k-1} - ay_k^2 + 1 = 0$$

highlights that for

$$\bar{\mu} = -\frac{1}{(1-b)RC} \tag{80}$$

they are exactly the same. Therefore, the discretization operator (A7) has induced a chaotic dynamics where the CT circuit could not exhibit any.

Figure 15 depicts the foliated phase-space of the memristive circuit described by (14) with Φ as in (17), when its configuration in normalized units of measure is as follows:

$$R = 2 \,, \quad C = 0.25 \,, \quad \gamma_1 = 0 \,, \quad \gamma_2 = \frac{a}{R(b-1)}$$
$$\gamma_3 = 0 \,, \quad a = 1.4 \,, \quad b = 0.3 \tag{81}$$

The trajectories generated for the same $\mu = -2.8571$ by two different solutions have been highlighted. The evolution of the one starting at the diamond has been reported in Fig. 16 along with the related DT sequences generated for different values of T by (73) with $\lambda = 0.7692$ according to (77). When T reaches the critical value (79) the corresponding first-return map of the DT sequence becomes as in Fig. 17A. Also the second-return map is portrayed in Figure 17B, that highlights the typical shape of the Henon strange attractor. In order to make the comparison of Fig. 16 meaningful, the initialization of the DT model has been taken in accordance to Corollary 5.

8 Conclusions

The paper has considered the class of continuous-time (CT) circuits composed by a linear time-invariant two-terminal element (one port) connected to a memristor, memcapacitor, or meminductor. These circuits are described by a nonlinear differential equation which admits first integrals and hence it enjoys the foliation feature of the phase-space. A discretization procedure of the differential equation has been devised with the goal of obtaining DT maps preserving this foliation feature. Specifically, the procedure consists on replacing the time derivative operator with a discretization operator belonging to a large family, including classic ones as Forward Euler, Backward Euler, and Tustin methods

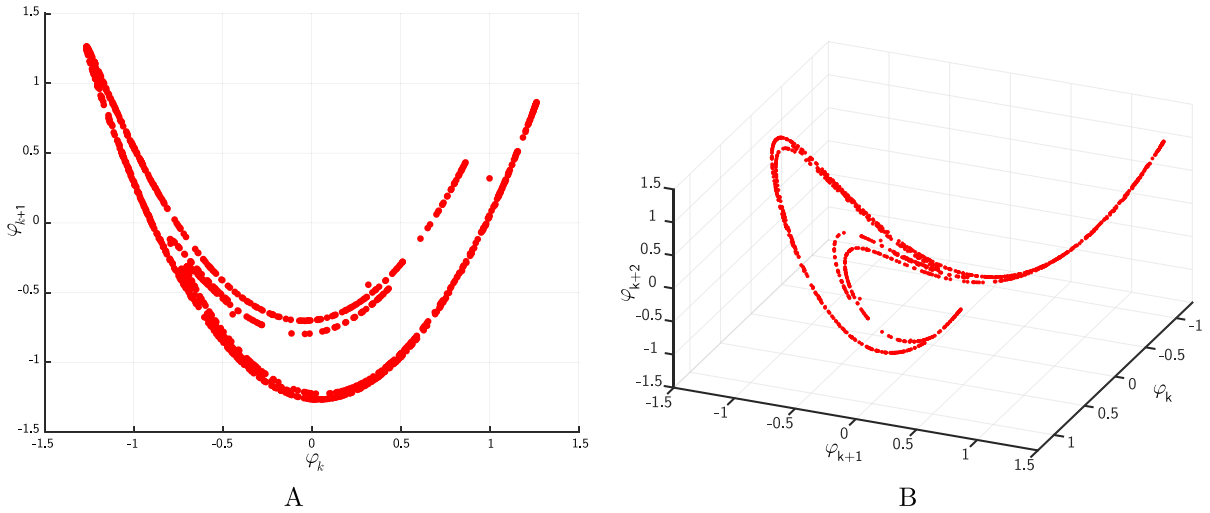

Fig. 17 First-return map (left) and second-return map (right) of the DT solution of (78) for $T = 0.269$, that satisfies condition (79)

as well as single-stage multi-step, multi-stage single-step, and averaging techniques. It has been shown that the obtained DT maps preserve the foliation feature of the original CT circuits for any discretization time step T. Hence, the phase-space of these maps is composed by a continuum of invariant manifolds, thus making it possible the coexistence of many different attractors, as well as extreme multistability, even in cases where the memelement characteristic is not of the sine type. Moreover, the influence of the time step T on the maps dynamics has been investigated, by showing that non-chaotic CT systems may become chaotic when discretized with a sufficiently large T, a phenomenon which is known as computational chaos. Notably, it is shown that a simple RC-memristive circuit, where the charge of a memristor depends quadratically on the flux, can exactly display the dynamics of the logistic and the Henon maps when the time-derivative operator is replaced by the discretization operators generated by the Forward Euler and the operator obtained by averaging the Forward and Backward Euler Methods, respectively, and the time step T is suitably chosen.
Future research will be devoted to investigate how the input-output appproach can be suitably extended to CT circuits having more than one memelements, a case where the state space approach currently seems to be more tractable from a computational standpoint.

Author contributions All authors contributed to the conceptualization of the work. G.I. and A.T. developed the methodology and the formal analysis, wrote the original draft, and reviewed and edited the final manuscript. M.D.M., L.P., and M.F. reviewed and edited the final manuscript.

Funding Not applicable.

Data Availability Statement The manuscript has no associated data and materials.

Declarations

Competing interests All the authors declare that they have no competing interests as defined by Springer, or other interests that might be perceived to influence the results and/or discussion reported in this paper.

Appendix A Derivation of the discretization operators

In this appendix the derivations of the discretization operators reported in Sections 5.2 and 5.3 are explained along with some illustrative examples.

A.1 Numerical integration methods

These methods are based on the observation that equation (1), i.e., $\mathcal{D}f(t) = g(t)$, is a differential equation, and, therefore, numerical integration techniques are suitable ways to approximate it. However, for the sake of Proposition 3 and Theorem 4, the corresponding discretization operators should satisfy Assumptions 2 and 3. As illustrated hereafter, the following standard integration methods provide operators ensuring these assumptions hold.

A.1.1 Forward Euler Method

The Forward Euler Method is a classic and very well-known numerical integration technique that approximates the differential equation (1) considering the related integral relationship

$$\begin{aligned}\mathcal{D}_{[t]}^{-1} g(t+T) &= \int_t^{t+T} g(\tau)d\tau \\ &= f(t+T) - f(t) = (h_T - 1) f(t)\end{aligned} \tag{A1}$$

and then using the rule

$$\mathcal{D}_{[t]}^{-1} g(t+T) \approx g(t)T \tag{A2}$$

to remove the integral on the left-hand side. From the geometrical point of view, equation (A2) says that the area subtended by function g over $[t, t+T]$ is approximated with the area of the rectangle with base T and height $g(t)$, i.e., evaluated at the starting instant of the interval. This is equivalent to replace the integrand function g over the interval $(t, t+T)$ with the function constant at the value $g(t)$. Using (A2) into (A1) leads to

$$\mathcal{D}f(t) = g(t) \approx \frac{h_T - 1}{T} f(t).$$

Therefore, this integration technique implies that the derivative operator is approximated by the discretization operator (43) of Table 3, that is here reported for the sake of clarity:

$$\Delta(T, h_T) = \frac{h_T - 1}{T} .$$

Notice that this result can also be derived from the Taylor development of function f

$$\begin{aligned} f(t+T) &= f(t) + T\mathcal{D}f(t) + o(T) \\ &= f(t) + Tg(t) + o(T) , \end{aligned}$$

which also highlights that the approximation error is a little-o of T.

A.1.2 Backward Euler Method

The Backward Euler Method approximates integral (A1) using the rule

$$\mathcal{D}_{[t]}^{-1} g(t+T) \approx g(t+T)T = h_T g(t)T$$

that, from the geometrical point of view, is equivalent to use the area of the rectangle of base T and height $g(t+T)$ in place of the area subtended by function g over $[t, t+T]$. Proceeding as before, we get the discretizazion operator $\Delta(T, h_T)$ in equation (44) of Table 3. This rule can also be derived using the Taylor development of function f just by observing that

$$\begin{aligned} f(t) &= f(t+T) - T\mathcal{D}f(t+T) + o(T) \\ &= h_T f(t) - Th_T g(t) + o(T) , \end{aligned}$$

which highlights that the approximation error is again a little-o of T.

A.1.3 Theta Method

The Theta Method can be seen as a parametric advancement of the Euler's methods. Indeed, given a parameter $\theta \in [0, 1]$, it approximates integral (A1) substituting the integrand function with a constant function that can be set at any of the possible values between $g(t)$ and $g(t+T)$ depending on θ:

$$\begin{aligned} \mathcal{D}_{[t]}^{-1} g(t+T) &\approx \big((1-\theta)g(t+T) + \theta g(t)\big)T \\ &= T\big((1-\theta)h_T + \theta\big)g(t) . \end{aligned}$$

Then, the corresponding approximation of the derivative becomes

$$\Delta(T, h_T) = \frac{1}{T} \frac{h_T - 1}{(1-\theta)h_T + \theta} ,$$

as reported in equation (45) of Table 3.

A.1.4 Midpoint Rule or Modified Euler Method

The Midpoint Rule approximates the integral

$$\begin{aligned}\mathcal{D}^{-1}_{[t-T]}g(t+T) &= \int_{t-T}^{t+T} g(\tau)d\tau \\ &= f(t+T) - f(t-T) \\ &= \left(h_T - h_T^{-1}\right) f(t) \\ &= \frac{h_T^2 - 1}{h_T} f(t)\end{aligned}$$

using the rule

$$\mathcal{D}^{-1}_{[t-T]}g(t+T) \approx g(t)2T \ . \tag{A3}$$

From the geometrical point of view, equation (A3) represents the area of the rectangle of base $2T$ and height $g(t)$. Thus, the discretization operator is given by

$$\Delta(T, h_T) = \frac{h_T - h_T^{-1}}{2T} = \frac{h_T^2 - 1}{2Th_T} \ , \tag{A4}$$

that is equation (46) of Table 3. This technique is very similar to the Euler's methods, because it replaces the integrand function with the constant value taken at the midpoint of the integrating interval $[t - T, t + T]$, which explains the name of the method. A different way to derive (A4) is to compute the average between the approximations given by the left and right incremental ratios centered in t:

$$\begin{aligned}g(t) = \mathcal{D}f(t) &\approx \frac{f(t+T) - f(t-T)}{2T} \\ &= \frac{1}{2}\frac{f(t+T) - f(t)}{T} \\ &\quad + \frac{1}{2}\frac{f(t) - f(t-T)}{T} \\ &= \frac{h_T - 1}{2T} + \frac{1 - h_T^{-1}}{2T} \\ &= \frac{h_T - 1}{2T} + \frac{h_T - 1}{2Th_T} = \frac{h_T^2 - 1}{2Th_T} f(t) \ .\end{aligned}$$

A.1.5 Tustin Method or Trapezoidal Rule

In the Tustin Method $\mathcal{D}^{-1}_{[t]}g(t+T)$ is computed by replacing the integrand function g with the segment connecting the points $\big(t, g(t)\big)$ and $\big(t+T, g(t+t)\big)$. This way the area subtended by g over $[t, t+T]$ is approximated by the area of a trapezoid:

$$\begin{aligned}\mathcal{D}^{-1}_{[t]}g(t+T) &= f(t+T) - f(t) \\ &\approx \frac{1}{2}\big(g(t) + g(t+T)\big)T \ .\end{aligned}$$

The corresponding discretization operator is

$$\Delta(T, h_T) = \frac{2}{T}\frac{h_T - 1}{h_T + 1} \ ,$$

that is equation (47) of Table 3.

A.2 Single-stage multi-step methods

These methods exploit interpolation techniques to approximate function f using a function properly chosen in a certain parametric class $\left\{v_p\right\}_{p\in\mathbb{R}^i}$, where p denotes the vector of the parameters and $i \in \mathbb{Z}_+$ is such that $i > 1$. The basic procedure aims to fix p by imposing the passage from a sufficient number of points of the form $\big(t + jT, f(t + jT)\big)$, where usually $j \in J = (-m, \ldots, -1, 0, 1, \ldots, n)$ and $m+n+1 = i$. This way, the vector of the parameters depends on the samples of f, i.e.,

$$p = p\big(T, f(t - mT), \ldots, f(t + nT)\big)$$

The methods are denoted as "multi-steps", because they use $i > 1$ points, and "single-stage", because all the points are distant T. Now, let $v_p(t) = v(t, p) = v\big(t, T, f(t-mT), \ldots, f(t+nT)\big)$ be the sought interpolating function of f. The procedure dictates to analytically compute the derivative $\mathcal{D}v(v, p) = w(t, p) = w\big(t, T, f(t-mT), \ldots, f(t+nT)\big)$ and to impose the approximation

$$\mathcal{D}f(t) \approx w\big(t, T, h_T^{-m}f(t), \ldots, h_T^n f(t)\big) \ .$$

If the above equation can be formulated (at least formally) as

$$\mathcal{D}f(t) \approx W\big(T, h_T^{-m}, \ldots, h_T^n\big)f(t)$$

for some proper operator W, then, the discretization operator assumes the form

$$\Delta(T, h_T) = W\left(T, h_T^{-m}, \ldots, h_T^{n}\right)$$

and it only remains to check if Assumptions 2 and 3 are satisfied.
For example, assume that around t the local interpolation function belongs to the parabola class

$$v_p(t+\tau) = a\tau^2 + b\tau + c\,,$$

where τ is the temporal displacement from t and $p = [a, b, c]^T \in \mathbb{R}^3$. Using as interpolation points $\big(t - T, f(t-T)\big)$, $\big(t, f(t)\big)$ e $\big(t+T, f(t+T)\big)$, i.e., $m = n = 1$ and $i = m+n+1 = 3$, the problem boils down to find a, b, and c such that

$$\begin{aligned} v_p(t) &= c = f(t) \\ v_p(t-T) &= aT^2 - bT + c = f(t-T) = h_T^{-1} f(t) \\ v_p(t+T) &= aT^2 + bT + c = f(t+T) = h_T f(t)\,. \end{aligned}$$

It can be readily verified that the above equations are solved for

$$\begin{aligned} a &= \frac{h_T - 2 + h_T^{-1}}{2T^2} f(t)\,, \quad b = \frac{h_T - h_T^{-1}}{2T} f(t) \\ c &= f(t)\,. \end{aligned}$$

Then, observing that

$$\begin{aligned} \mathcal{D}v_p(t) &= \left.\frac{dv_p(t+\tau)}{d\tau}\right|_{\tau=0} = [2a\tau + b]_{\tau=0} \\ &= b = \frac{h_T - h_T^{-1}}{2T} f(t) \approx \mathcal{D}f(t) \end{aligned}$$

it finally follows that

$$\Delta(T, h_T) = \frac{h_T - h_T^{-1}}{2T}\,,$$

which is exactly the Midpoint Rule.

A.3 Multi-stage single-step methods

These techniques are based on local interpolation problems just as in the single-stage multi-step case, but in this case they are applied to the integrand function g instead of f, and the points of its graph used for the interpolation are taken within a "single-step", i.e., inside the unique interval ranging from t to $t+T$, that is, therefore, divided into a "multi-stage" partition. Then, the function interpolating g is then used to compute the integral $\mathcal{D}_{[t]}^{-1} g(t+T)$, as already done to derive the discretization operator of Appendix A.1. Nonetheless, the interpolating function depends on samples that are not taken using the step T, and therefore the application of the related discretization operator to build a DT map requires an additional machinery that depends on the specific case. It is worth observing that the Simpson's Rule is an example of this approach [47], and that also the Runge-Kutta methods [44] use a similar mechanism extended with a procedure to predict the points in the middle of the step interval.

A simple way to illustrate the above approach consists in approximating g with a parametric piece-wise linear function w_p that interpolates it in the points $\big(t, g(t)\big)$, $\Big(t + \frac{T}{2}, g\big(t + \frac{T}{2}\big)\Big)$, and $\big(t+T, g(t+T)\big)$. Proceeding this way, it follows that

$$\begin{aligned} (h_T - 1) f(t) &= f(t+T) - f(t) = \int_t^{t+T} g(\tau) d\tau \\ &\approx \int_t^{t+T} w_p(\tau) d\tau \\ &= \frac{T}{2} \frac{g(t) + g\big(t + \frac{T}{2}\big)}{2} + \frac{T}{2} \frac{g\big(t + \frac{T}{2}\big) + g(t+T)}{2} \\ &= \frac{T}{4} \left(g(t) + 2g\left(t + \frac{T}{2}\right) + g(t+T) \right) \\ &= \frac{T}{4} \left(h_T^0 + 2h_T^{\frac{1}{2}} + h_T^1 \right) g(t)\,, \end{aligned}$$

where $h_T^{\frac{1}{2}} = \sqrt{h_T}$ is such that $\sqrt{h_T} g(t) = g\big(t + \frac{T}{2}\big)$, and it extends the definition of shift operator, because $(\sqrt{h_T})^2 g(t) = g(t+T) = h_T g(t)$. Then, the corresponding discretization operator is

$$\Delta\left(T, h_T^0, h_T^{\frac{1}{2}}, h_T^1\right) = \frac{4}{T} \frac{h_T - 1}{h_T^0 + 2h_T^{\frac{1}{2}} + h_T^1}\,. \tag{A5}$$

The numerator of (A5) reveals that all the techniques of this class which are designed from the integral relationship (A1) satisfy Assumption 3.

Finally, we observe that the use of the discretization operators of this class often requires a compli-

cated machinery to conceive a proper definition of the DT variable x_k, because of the possible presence of operators h_T^j with non integer values of j, which usually need auxiliary coordinates, that may be time-shifted or related to different sampling rates. However, in the above example, the design of a DT map using operator (A5) can be done exploiting a simple trick, that ensures the satisfaction of Assumption 2 too. Indeed, if the DT variable is created by substituting $x_k \leftarrow x\left(t + k\frac{T}{2}\right)$, then all the necessary samples, the intermediate ones included, already corresponds to integer values of k. Therefore, using a proper "oversampling" has prevented the introduction of an additional auxiliary variable. This solution can always be exploited to solve the problem, but it limits the choice of the sampling instants.

A.4 Averaging techniques

The averaging techniques are a simple but effective way to design more refined approximations of $\mathcal{D}$ by "mixing" together a number of already known discretization operators, which already satisfy Assumptions 2 and 3. They can be formulated by considering $n > 1$ discretization operators $\Delta_i(T, h_T)$, $i = 1, \ldots, n$, and computing their weighted mean:

$$\Delta(T, h_T) = \frac{1}{\sum_{i=1}^{n} \lambda_i} \sum_{i=1}^{n} \lambda_i \Delta_i(T, h_T) \tag{A6}$$

for a given set of weights $\lambda_i \in \mathbb{R}$, $\lambda_i > 0$, $i = 1, \ldots, n$. Then, the corresponding operator (A6) can exhibit to a certain extent features deriving from the single $\Delta_i(T, h_T)$. For instance, consider the following weighted mean between the Forward and Backward Euler methods

$$\begin{aligned} \Delta(T, h_T) &= \lambda \frac{h_T - 1}{T} + (1 - \lambda) \frac{h_T - 1}{T h_T} \\ &= \frac{\lambda h_T^2 + (1 - 2\lambda) h_T - (1 - \lambda)}{T h_T} \end{aligned} \tag{A7}$$

for $\lambda \in [0, 1]$. Notice that for $\lambda = 0, \lambda = \frac{1}{2}, \lambda = 1$ this technique boils down to the Backward Euler Method, the Midpoint Rule, and the Forward Euler Method, respectively. Since both of the Euler methods satisfy Assumptions 2 and 3, discretization operator (A7) satisfies them both.

References

1. Chua, L.O.: Memristor-The missing circuit element. IEEE Trans. Circuit Theory **18**(5), 507–519 (1971)
2. Strukov, D.B., Snider, G.S., Stewart, D.R., Williams, R.S.: The missing memristor found. Nature **453**(7191), 80 (2008)
3. Di Ventra, M., Pershin, Y.V., Chua, L.O.: Circuit elements with memory: memristors, memcapacitors, and meminductors. Proc. IEEE **97**(10), 1717–1724 (2009)
4. Yang, J.J., Williams, R.S.: Memristive devices in computing system: Promises and challenges. ACM Journal on Emerging Technologies in Computing Systems (JETC) **9**(2), 1–20 (2013)
5. Williams, R.S.: What's Next? [The end of Moore's law]. Computing in Science & Engineering **19**(02), 7–13 (2017). https://doi.org/10.1109/MCSE.2017.31
6. Sebastian, A., Le Gallo, M., Burr, G.W., Kim, S., BrightSky, M., Eleftheriou, E.: Tutorial: Brain-inspired computing using phase-change memory devices. J. Appl. Phys. **124**(11), 111101 (2018). https://doi.org/10.1063/1.5042413
7. James, A.P., Salama, K.N., Li, H., Biolek, D., Indiveri, G., Chua, L.O.: Guest editorial: Special issue on large-scale memristive systems and neurochips for computational intelligence. IEEE Transactions on Emerging Topics in Computational Intelligence **2**(5), 320–323 (2018). https://doi.org/10.1109/TETCI.2018.2867375
8. Huang, T., Chen, Y., Zeng, Z., Chua, L.O.: Editorial special issue for 50th birthday of memristor theory and application of neuromorphic computing based on memristor-part I. IEEE Trans. Circuits Syst. I Regul. Pap. **68**(11), 4417–4418 (2021). https://doi.org/10.1109/TCSI.2021.3115842
9. Sirakoulis, G.C., Ascoli, A., Tetzlaff, R., Yu, S.: Guest editorial memristive circuits and systems for edge-computing applications. IEEE Journal on Emerging and Selected Topics in Circuits and Systems **12**(4), 717–722 (2022). https://doi.org/10.1109/JETCAS.2022.3226900
10. Itoh, M., Chua, L.O.: Memristor oscillators. International Journal on Bifurcations and Chaos **18**(11), 3183–3206 (2008)
11. Buscarino, A., Fortuna, L., Frasca, M., Gambuzza, L.V.: A gallery of chaotic oscillators based on HP memristor. International Journal of Bifurcation and Chaos **23**(05), 1330015 (2013). https://doi.org/10.1142/S0218127413300152
12. Kumar, S., Strachan, J.P., Williams, R.S.: Chaotic dynamics in nanoscale NbO2 Mott memristors for analogue computing. Nature **548**, 318–321 (2017). https://doi.org/10.1038/nature23307
13. Liang, Y., Wang, G., Chen, G., Dong, Y., Yu, D., Iu, H.H.-C.: S-type locally active memristor-based periodic and chaotic oscillators. IEEE Trans. Circuits Syst. I Regul. Pap. **67**(12), 5139–5152 (2020). https://doi.org/10.1109/TCSI.2020.3017286
14. Ascoli, A., Demirkol, A.S., Tetzlaff, R., Chua, L.: Edge of chaos theory resolves Smale paradox. IEEE Trans. Circuits Syst. I Regul. Pap. **69**(3), 1252–1265 (2022). https://doi.org/10.1109/TCSI.2021.3133627
15. Ascoli, A., Demirkol, A.S., Tetzlaff, R., Chua, L.O.: Edge of chaos explains Prigogine's instability of the homogeneous. IEEE Journal on Emerging and Selected Topics in

Circuits and Systems **12**(4), 804–820 (2022). https://doi.org/10.1109/JETCAS.2022.3221156
16. Corinto, F., Forti, M., Chua, L.O., et al.: Nonlinear circuits and systems with memristors. Springer, Cham, Switzerland (2021)
17. Innocenti, G., Tesi, A., Di Marco, M., Forti, M.: First integrals can explain coexistence of attractors, multistability, and loss of ideality in circuits with memristors. Chaos, Solitons Fractals **180**, 114504 (2024). https://doi.org/10.1016/j.chaos.2024.114504
18. Di Marco, M., Innocenti, G., Tesi, A., Forti, M.: Circuits with a mem-element: invariant manifolds control via pulse programmed sources. Nonlinear Dyn. **106**, 2577–2606 (2021)
19. Hens, C.R., Banerjee, R., Feudel, U., Dana, S.K.: How to obtain extreme multistability in coupled dynamical systems. Phys. Rev. E **85**, 035202 (2012). https://doi.org/10.1103/PhysRevE.85.035202
20. Bao, B.-C., Xu, Q., Bao, H., Chen, M.: Extreme multistability in a memristive circuit. Electron. Lett. **52**(12), 1008–1010 (2016). https://doi.org/10.1049/el.2016.0563
21. Corinto, F., Forti, M.: Memristor Circuits: Bifurcations without Parameters. IEEE Trans. Circuits Syst. I, Reg. Papers **64**(6), 1540–1551 (2017)
22. Chang, H., Li, Y., Yuan, F., Chen, G.: Extreme multistability with hidden attractors in a simplest memristor-based circuit. International Journal of Bifurcation and Chaos **29**(06), 1950086 (2019). https://doi.org/10.1142/S021812741950086X
23. Itoh, M., Chua, L.: Memristor Cellular Automata and Memristor Discrete-Time Cellular Neural Networks, pp. 1289–1361. Springer, Cham (2019)
24. Solan, E., Ochs, K.: Wave digital emulation of general memristors. Int. J. Circuit Theory Appl. **46**(11), 2011–2027 (2018)
25. Xu, B., Zou, S., Bai, L., Chen, K., Zhao, J.: A general discrete memristor emulator based on Taylor expansion for the reconfigurable FPGA implementation and its application. Nonlinear Dyn. **112**(2), 1395–1414 (2024)
26. Bao, B.-C., Li, H., Wu, H., Zhang, X., Chen, M.: Hyperchaos in a second-order discrete memristor-based map model. Electron. Lett. **56**(15), 769–770 (2020). https://doi.org/10.1049/el.2020.1172
27. Peng, Y., Sun, K., He, S.: A discrete memristor model and its application in hénon map. Chaos, Solitons & Fractals **137**, 109873 (2020)
28. Li, H., Hua, Z., Bao, H., Zhu, L., Chen, M., Bao, B.: Two-dimensional memristive hyperchaotic maps and application in secure communication. IEEE Trans. Industr. Electron. **68**(10), 9931–9940 (2020)
29. Bao, H., Hua, Z., Li, H., Chen, M., Bao, B.: Discrete memristor hyperchaotic maps. IEEE Trans. Circuits Syst. I Regul. Pap. **68**(11), 4534–4544 (2021)
30. Deng, Y., Li, Y.: Nonparametric bifurcation mechanism in 2-D hyperchaotic discrete memristor-based map. Nonlinear Dyn. **104**(4), 4601–4614 (2021)
31. Bao, H., Gu, Y., Xu, Q., Zhang, X., Bao, B.: Parallel bi-memristor hyperchaotic map with extreme multistability. Chaos, Solitons & Fractals **160**, 112273 (2022)
32. Bao, H., Li, H., Hua, Z., Xu, Q., Bao, B.: Sine-transform-based memristive hyperchaotic model with hardware implementation. IEEE Trans. Industr. Inf. **19**(3), 2792–2801 (2022)
33. Ma, M., Yang, Y., Qiu, Z., Peng, Y., Sun, Y., Li, Z., Wang, M.: A locally active discrete memristor model and its application in a hyperchaotic map. Nonlinear Dyn. **107**(3), 2935–2949 (2022)
34. Zhang, S., Zhang, H., Wang, C.: Dynamical analysis and applications of a novel 2-D hybrid dual-memristor hyperchaotic map with complexity enhancement. Nonlinear Dyn. **111**(16), 15487–15513 (2023)
35. Lai, Q., Yang, L., Chen, G.: Design and performance analysis of discrete memristive hyperchaotic systems with stuffed cube attractors and ultraboosting behaviors. IEEE Trans. Industr. Electron. **71**(7), 7819–7828 (2023)
36. Li, Y., Wang, M., Chang, H., Wang, H., Chen, G.: A hyperchaotic memristive system with extreme multistability and conservativeness. Nonlinear Dyn. **112**(5), 3851–3868 (2024)
37. Hussan, I., Zhao, M., Zhang, X.: Two-memristor-based maps with infinitely many hyperchaotic attractors. Chaos, Solitons & Fractals **191**, 115904 (2025)
38. Di Marco, M., Forti, M., Pancioni, L., Tesi, A.: New class of discrete-time memristor circuits: first integrals, coexisting attractors and bifurcations without parameters. International Journal of Bifurcation and Chaos **34**(01), 2450001 (2024)
39. Di Marco, M., Forti, M., Pancioni, L., Tesi, A.: Snap-back repellers, computational chaos and extreme multistability in discrete-time memristor Murali–Lakshmanan–Chua circuit. International Journal of Bifurcation and Chaos **34**(11), 2430022 (2024). https://doi.org/10.1142/S0218127424300222
40. Di Marco, M., Forti, M., Pancioni, L., Tesi, A.: Snap-back repellers and chaos in a class of discrete-time memristor circuits. Nonlinear Dyn. **112**(15), 13519–13537 (2024)
41. Di Marco, M., Forti, M., Pancioni, L., Innocenti, G., Tesi, A.: Embedding classic chaotic maps in simple discrete-time memristor circuits. IEEE Access (2024)
42. Innocenti, G., Di Marco, M., Tesi, A., Forti, M.: Input-output characterization of the dynamical properties of circuits with a memelement. International Journal of Bifurcation and Chaos **30**(07), 2050110 (2020)
43. Lorenz, E.N.: Computational chaos - a prelude to computational instability. Physica D **35**(3), 299–317 (1989)
44. Butcher, J.C.: Numerical Methods for Ordinary Differential Equations. John Wiley & Sons, West Sussex, UK (2016). https://doi.org/10.1002/9781119121534
45. Leader, J.J.: Numerical Analysis and Scientific Computation. Chapman and Hall/CRC Press, Abingdon, Oxon, UK (2022)
46. Strogatz, S.H.: Nonlinear Dynamics and Chaos with Student Solutions Manual: With Applications to Physics, Biology, Chemistry, and Engineering. CRC Press, Abingdon, Oxon, UK (2018)
47. Süli, E., Mayers, D.F.: An Introduction to Numerical Analysis. Cambridge University Press, Canada (2003)